



HAL
open science

Genesis of Carbonatite at Oldoinyo Lengai (Tanzania) from Olivine Nephelinite: Protracted Melt Evolution and Reactive Porous Flow in Deep Crustal Mushes

Adrien J Mourey, Lydéric France, Benoît Ildefonse, Andrey Gurenko, Didier
Laporte

► **To cite this version:**

Adrien J Mourey, Lydéric France, Benoît Ildefonse, Andrey Gurenko, Didier Laporte. Genesis of Carbonatite at Oldoinyo Lengai (Tanzania) from Olivine Nephelinite: Protracted Melt Evolution and Reactive Porous Flow in Deep Crustal Mushes. *Journal of Petrology*, 2023, 64 (12), pp.1-24. 10.1093/petrology/egad084 . hal-04373738

HAL Id: hal-04373738


<https://hal.science/hal-04373738v1>

Submitted on 5 Jan 2024

HAL is a multi-disciplinary open access archive for the deposit and dissemination of scientific research documents, whether they are published or not. The documents may come from teaching and research institutions in France or abroad, or from public or private research centers.

L'archive ouverte pluridisciplinaire **HAL**, est destinée au dépôt et à la diffusion de documents scientifiques de niveau recherche, publiés ou non, émanant des établissements d'enseignement et de recherche français ou étrangers, des laboratoires publics ou privés.

Genesis of Carbonatite at Oldoinyo Lengai (Tanzania) from Olivine Nephelinite: Protracted Melt Evolution and Reactive Porous Flow in Deep Crustal Mushes

Adrien J. Mourey ^{1,*}, Lydéric France ^{2,3}, Benoît Ildefonse⁴, Andrey Gurenko² and Didier Laporte⁵

¹Earth Observatory of Singapore, Nanyang Technological University, Singapore, Singapore

²Université de Lorraine, CNRS, CRPG, F-54000 Nancy, France

³Institut Universitaire de France (IUF), France

⁴Géosciences Montpellier, University of Montpellier, CNRS, Montpellier, France

⁵University Clermont-Auvergne, CNRS, IRD, OPGC, Laboratoire Magmas et Volcans, Clermont-Ferrand, France

*Corresponding author email address: admourey@gmail.com; adrien.mourey@ntu.edu.sg

Abstract

Carbonatites, carbon-rich magmatic rocks, are thought to form by low-degree partial melting of a relatively carbon-poor mantle followed by protracted differentiation and immiscibility. However, the nature of parental magmas and the characteristics of the early stages of differentiation that shape the subsequent crystal and liquid lines of descent remain poorly constrained. To provide new constraints, deep crustal cumulative xenoliths from Oldoinyo Lengai (East African Rift), the only active volcano erupting carbonatite magmas, were studied. We use major and volatile elements in primitive olivine-hosted melt inclusions, as well as major and trace elements in crystals, to reconstruct the conditions of formation and evolution of cumulates (pressure, temperature, composition). Xenoliths are composed of olivine, diopside, phlogopite, amphibole and accessory minerals. One remarkable feature is the presence of diopside and phlogopite oikocrysts enclosing roundish olivine chadacrysts. Melt inclusions do not have vapor bubble and have major element compositions resembling olivine nephelinite (7–10 wt % MgO after corrections for post-entrapment crystallization). The absence of vapor bubbles implies that the concentrations of volatile components (i.e. CO₂, H₂O, S) were not compromised by well-known post-entrapment volatile loss into the vapor bubble. Based on the melt inclusion study by SIMS, the volatile concentrations in olivine nephelinite magmas (early stage of differentiation) at Oldoinyo Lengai were 20–130 ppm S, 390–4500 ppm F, 50–540 ppm Cl, up to 6074 ppm CO₂ and up to 1.5 wt % H₂O. According to the calculated CO₂-H₂O saturation pressures and geophysical data, xenoliths from Embalulu Oltatwa document a mushy reservoir in the lower crust. Primitive olivine nephelinite melt inclusions have higher H₂O contents than olivine nephelinite lavas from other further South volcanoes from the North Tanzanian Divergence (0.2–0.5 wt % H₂O), suggesting that the lithospheric mantle source beneath the Oldoinyo Lengai is more hydrated than the mantle beneath the rest of North Tanzanian Divergence. We present a model in which resorption features observed in olivine chadacrysts, together with the LREE enrichments in olivine grains, are the consequences of reactive porous flows in a deep crustal mushy reservoir. We provide constraints on the major, trace and volatile element composition of the parental magmas of carbonatite series and demonstrate with Rhyolite-MELTS models that phonolites and related natrocarbonatites from Oldoinyo Lengai can be produced by protracted differentiation of olivine nephelinite melts.

INTRODUCTION

Although relatively rare, carbonatite magmas have been recorded throughout Earth's History (Woolley & Kjarsgaard, 2008) in association with alkali-rich silicate magmas. Carbonatite magmas and associated alkaline-rich silicate magmas represent nowadays the main Rare Earth Elements deposits on Earth (e.g. Verplanck *et al.*, 2014), and deciphering their genesis and evolution remains a challenge in igneous petrology. The origin of such magmas is debated, and two main models are opposed. Carbonatites are either formed directly by the melting of a C-rich mantle domain (e.g. Wallace & Green, 1988; Hammouda *et al.*, 2014), or by immiscibility from an evolved alkaline silicate melt that is the ultimate product of a protracted differentiation series (e.g. Peterson, 1989; Dawson, 1992; Fischer *et al.*, 2009; Mollex *et al.*, 2018; Casola *et al.*, 2020; Nabyl *et al.*, 2020; France *et al.*, 2021). In the latter case, very low degrees of partial melting of a C-poor mantle source are likely

required to form the parental magmas (Hirschmann, 2010; Stamm & Schmidt, 2017). In any case, the nature of the parental magmas of the carbonatite series, their volatile content and the related characteristics of the differentiation series (both liquid and crystal lines of descent) need to be constrained. Here we provide new constraints from the Oldoinyo Lengai igneous system.

The Oldoinyo Lengai stratovolcano (East African Rift, Northern Tanzania) is the only active volcano that erupts natrocarbonatites, thus representing a unique opportunity to study the genesis of carbonatites and related alkaline series. The parental melts at the origin of the protracted differentiation series are likely olivine melilitites and/or olivine nephelinites (e.g. Dawson, 1998, 2012; Keller *et al.*, 2006). These melts, once highly differentiated, would eventually produce conjugate alkaline carbonatites and silicate melts (phonolites to alkaline nephelinites; Mitchell, 2009; France *et al.*, 2021). Nevertheless, very little is known about the liquid and

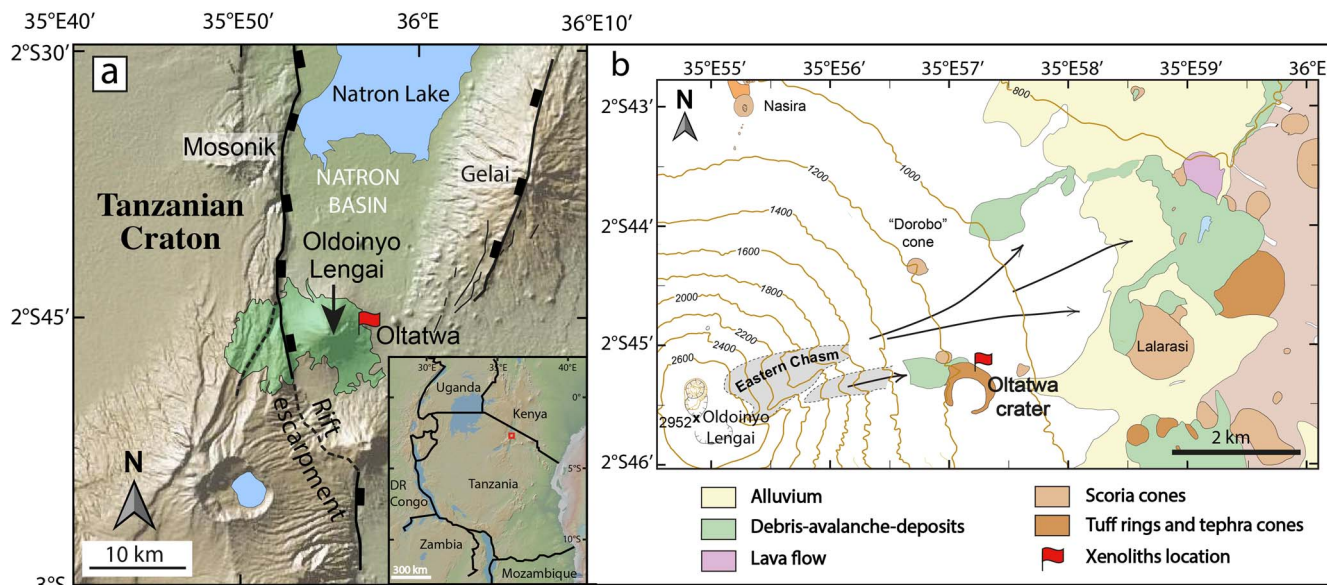


Fig. 1. (a) Topographic map of the Natron lake magmatic province (<http://www.geomapp.org>, topography data from Ryan *et al.*, 2009). The delimited area around the volcano represents the distribution of tephras of the 2007–2008 eruption (Bosshard-Stadlin *et al.*, 2014); (b) Geological map with location of maar Embalulu Oltatwa and samples on the east-northeast flank of Oldoinyo Lengai (modified from Sherrod *et al.*, 2013).

cumulate lines of descent of melilitites and olivine nephelinites and about the deep crustal igneous processes governing the differentiation series. Here, by using xenoliths of deep cumulative samples crystallized from olivine nephelinite melts, we bring new constraints on the parental magma composition (major, trace and volatile elements), and on the igneous processes involved in the transfer of primitive melts in deep crustal reservoirs. More specifically, we highlight the occurrence of reactive porous flow in deep crustal mushes and discuss the fate of those primitive magmas and their potential relation to the phonolite-carbonatite conjugate melts that have been reported in shallower mid-crust reservoirs (Mitchell, 2009; Bosshard-Stadlin *et al.*, 2014; France *et al.*, 2021).

Geological setting and xenolith samples

The Oldoinyo Lengai stratovolcano is part of the late Tertiary and Quaternary Natron lake magmatic province in northern Tanzania (Dawson, 2012). The volcano is in the Gregory Rift segment at ~16 km south of Natron Lake, in the East African rift system (Fig. 1a). It is located in an area where a rift segment controlled by a border fault and a developing magmatic rift segment are interacting (Roecker *et al.*, 2017). The oldest deposits are dated to 350 ka and are part of a phonolite cone (Lengai I) representing ~60% of the present-day edifice (Sherrod *et al.*, 2013). After a partial collapse of the edifice ~11 ka ago, an alkaline-nephelinite cone was created (Lengai II), representing ~35% of the present-day edifice (Klaudius & Keller, 2006). Although alkaline carbonatite lavas were likely already present during the Lengai I stage (France *et al.*, 2021), natrocarbonatite products, which are highly sensitive to weathering, are mainly present in the last century deposits. In addition to the long-lasting natrocarbonatite lava flow eruptions, several sub-Plinian alkaline nephelinite, phonolite and carbonatite eruptions occurred over the past century (eruptions in 1917, 1940–1941, 1966–1967, 2007–2008; Keller *et al.*, 2010; Kervyn *et al.*, 2010) each time creating craters several hectometers large that are subsequently progressively infilled with natrocarbonatite flows (Tournigand *et al.*, 2023).

Oldoinyo Lengai volcanic plumbing system and sampling

Previous geophysical and petrological investigations helped to refine the architecture of Oldoinyo Lengai's plumbing system. Two areas of magma or mush storage are inferred from geophysical data with potential connections between each other (Reiss *et al.*, 2021). The deep crustal reservoir is located in the lower crust (~25 ± 5 km below the surface) and is currently in a mushy state (Plasman *et al.*, 2017; Roecker *et al.*, 2017; Weinstein *et al.*, 2017). This deep reservoir regularly feeds a mid- to upper-crust reservoir that is located at depths of ~6 to 12 km (Weinstein *et al.*, 2017; Reiss *et al.*, 2021). The latter is connected to the surface through a complex mushy plumbing system composed of interconnected dikes and sills (Reiss *et al.*, 2021). Seismic data related to the last sub-Plinian explosive eruption at Oldoinyo Lengai highlight the reactivation of the mid-crust reservoir that first injected a dike toward Gelai volcano (Fig. 1a) before feeding the 2007 to 2008 Lengai eruption (Albaric *et al.*, 2010). These interpretations are consistent with the petrological record of the 2007 to 2008 eruption that suggests the recharge of alkaline nephelinites within the mid-crust reservoir with alkaline carbonatites and potential immiscible silicate melts (Bosshard-Stadlin *et al.*, 2014). Melt recharges by evolved alkaline nephelinite melts in the mid-crust reservoir imply that melt differentiation occurs at deeper levels, potentially within the lower crust mushy reservoir ~25 ± 5 km below the surface (e.g. Roecker *et al.*, 2017; Weinstein *et al.*, 2017).

The primitive volcanic products that erupted at the Natron lake magmatic province are mainly basanite, olivine melilitite and olivine nephelinite lavas (Mattsson *et al.*, 2013). Other primitive SiO₂-undersaturated melilitite magmas (with 29.4–33.5 wt % SiO₂, 4.0–5.9 wt % MgO and 16.3–24.4 wt % CaO) have been observed at the nearby Kerimasi volcano (Berkesi *et al.*, 2023). Mantle and rare cumulative xenoliths are observed in the deposits from several maars or cones near the Oldoinyo Lengai volcano, whose deposits locally contain up to 30 vol % xenoliths (Mattsson, 2012). The xenoliths likely sample different levels of the lithospheric mantle and of the magmatic plumbing

system. Here, we focus on four xenoliths from a 650 m diameter tuff ring named Embalulu Oltatwa on the lower east flank of Oldoinyo Lengai (~3 km from the summit; Fig. 1b). Embalulu Oltatwa crater formed 353 ± 65 ka ago ($^{40}\text{Ar}/^{39}\text{Ar}$ dating on phlogopite; Sherrod *et al.*, 2013), making this maar one of the oldest edifices of the Oldoinyo Lengai volcanic system; it has been partially infilled by debris-flow deposits and fallout tephra from Oldoinyo Lengai and by fluvial sand during rare rainy periods (Sherrod *et al.*, 2013). Pyroclastic deposits material comprises juvenile lapilli and ash with a melilititic composition as well as various cumulative xenoliths (Fig. 2a), free olivine and phlogopite crystals. The host lava, that carried the xenoliths at the Embalulu Oltatwa crater contains microlites (clinopyroxene 'Cpx', olivine, altered melilite, Mg-ferrierite, nepheline, euhedral and interstitial calcite), phenocrysts (olivine, Cpx, phlogopite) and accessory minerals (titanomagnetite, chromite, ulvöspinel, perovskite and pentlandite; Fig. 2b–c). We selected four representative cumulate xenoliths that were the largest available (4–15 cm in diameter): 14TL21, 14TL22a, 14TL22b and 14TL22e. Xenoliths were sampled in October 2014 on the North flank of the tuff ring Embalulu Oltatwa among pyroclastic deposits. These xenoliths are the most primitive cumulates described at Oldoinyo Lengai (Dawson *et al.*, 1995). The studied cumulates document the early stages of differentiation under Oldoinyo Lengai's carbonatitic complex. Petrographic observations were made on polished thin sections.

METHODS

Electron backscattered diffraction

Electron Backscattered Diffraction (EBSD) documents the crystallographic preferred orientation (CPO) and intracrystalline deformation (misorientation) for the various minerals. CPO are displayed as equal-area, lower hemisphere stereographic projections of average Euler angles for each grain to avoid over representation of large grains. CPO and intra-grain misorientation maps were acquired for the four studied xenoliths on polished thin sections. Measurements were performed using a JEOL-5600 Scanning Electron Microscope at Geosciences Montpellier laboratory (France). Measurements were performed on tilted thin sections (70° relative to the horizontal). Diffraction patterns were acquired using an acceleration voltage of 17 kV, and a working distance of 24 mm. AZtec software (Oxford instrument) has been used for the indexation of Kikuchi bands. Regular grid step between 15 to $30 \mu\text{m}$ for full thin sections ($30 \times 15 \text{ mm}$) was chosen to provide information on substructures and grain shapes. The indexation rate lies between 54 to 80%. Pole figures and maps were produced with the MTEX matlab toolbox (e.g. Mainprice *et al.*, 2014). Between 1100 and 4566 olivine grains and between 899 and 4026 Cpx grains have been indexed (an amount that is statistically representative of the sample). Raw data have been filtered to 1) discard pixels with mean angular deviations (i.e. the angle between the acquired diffraction pattern and the indexing solution) $< 1^\circ$, and 2) discard grains containing less than five pixels, which are considered as measurement errors. The strength of the fabric is quantified using the J index (e.g. Mainprice *et al.*, 2014), which varies from 1 for a random distribution to infinity for a single perfectly uniform crystal. Single grains are reconstructed by automatically selecting adjacent pixels with misorientations $< 10^\circ$. Intra-crystalline deformation is quantified using the Mis2Mean parameter that quantifies the misorientation of each pixel within a single grain with the mean orientation of the grain. We also calculated the GOS (Grain Orientation Spread), which is the average Mis2Mean

for each detected grain, and the shape factor (ratio between the grain perimeter and the equivalent perimeter).

Electron microprobe analysis

Major element concentrations (Si, Mg, Al, Fe, Na, K, Ca, Ti, Ni, Cr, Mn and P) were quantified by using a CAMECA SX-100 electron microprobe with five wavelength-dispersive spectrometers at the SCMEM (Université de Lorraine, France). Melt inclusions (MIs) were analyzed using an accelerating voltage of 15 kV and a probe current of 6 nA, with a defocused beam ($5 \mu\text{m}$). A focused beam with a current of 12 nA and an accelerating voltage of 15 kV was applied for all minerals. All analyses were performed with $K\alpha$ emissions for all elements. Counting times were 10 seconds for the background, 10 seconds for Na and K, and 20 seconds on the peaks for the other elements. Instrument calibration was performed on albite for Na, forsterite for Mg, hematite for Fe, corundum for Al, K-Orthoclase for K, vanadinite for Cl andradite for Ca, manganese(II) titanate for Mn and Ti, chromium(III) oxide for Cr, wollastonite for Si, NiO metal for Ni, apatite for P, barite for S and matrix correction was based on Pouchou & Pichoir (1991). Accuracy for all elements ($< 3\%$) is reported in the supplementary material.

X-ray and energy-dispersive spectroscopy (EDS) maps

X-ray intensity maps of Ti, Cr and P on thin sections were performed using an accelerating voltage of 15 kV and a current of ~ 500 nA by using a JEOL JXA-8230 electron probe microanalyzer at CRPG laboratory (Nancy, France). Dwell times per pixel were 200 ms and spatial resolution was $4 \times 4 \mu\text{m}$. Spatial resolution for zoomed P map of olivine is $1.5 \times 1.5 \mu\text{m}$. Along with X-ray intensity maps, EDS maps were acquired for Fe, Al, Ca, Na, Si and Mg. The P maps presented herein correspond to the sum of simultaneous measurements performed on three WDS spectrometers. The maps were extracted as raw intensity data that are converted into quantitative maps using spot analyses.

Laser ablation analysis

Trace element concentrations in minerals were quantified by laser ablation inductively coupled plasma mass spectrometry (LA-ICP-MS) at Geosciences Montpellier (France). The laser ablation system is a homogenized Ar-F Excimer Resonetics M-50E laser at 193 nm (Günther *et al.*, 1997) that is coupled with an Excimer CompEx102 with GeoLas Q+. The correction of the signal variation is based on the calibration values from Gagnon *et al.* (2008). The beam diameter was set at $122 \mu\text{m}$ for olivine, and $77 \mu\text{m}$ for the other minerals, with a laser pulse frequency of 7–10 Hz and a fluence of 12 J cm^{-2} . NIST 612 is used as an external standard and BIR-1 is used as an internal standard for minerals analysis. For trace element concentrations in minerals, SiO_2 and CaO serve as calibration. Data processing and reduction were conducted by using the Glitter Software (Van Achterbergh *et al.*, 2001). The corresponding data and associated analytical errors are available in the supplementary material.

Secondary ion mass spectrometry (SIMS)

In situ volatile concentrations in naturally quenched olivine-hosted melt inclusions were measured during two five-day-long analytical sessions in March and April 2017 with the CAMECA IMS 1280 HR2 ion microprobe at CRPG (Nancy, France). The inclusion-bearing olivine grains were analyzed for volatiles by SIMS before EPMA analysis to avoid contamination due to carbon coating. Individual olivine grains containing natural MIs were picked and mounted in epoxy. The grains were gently ground and polished

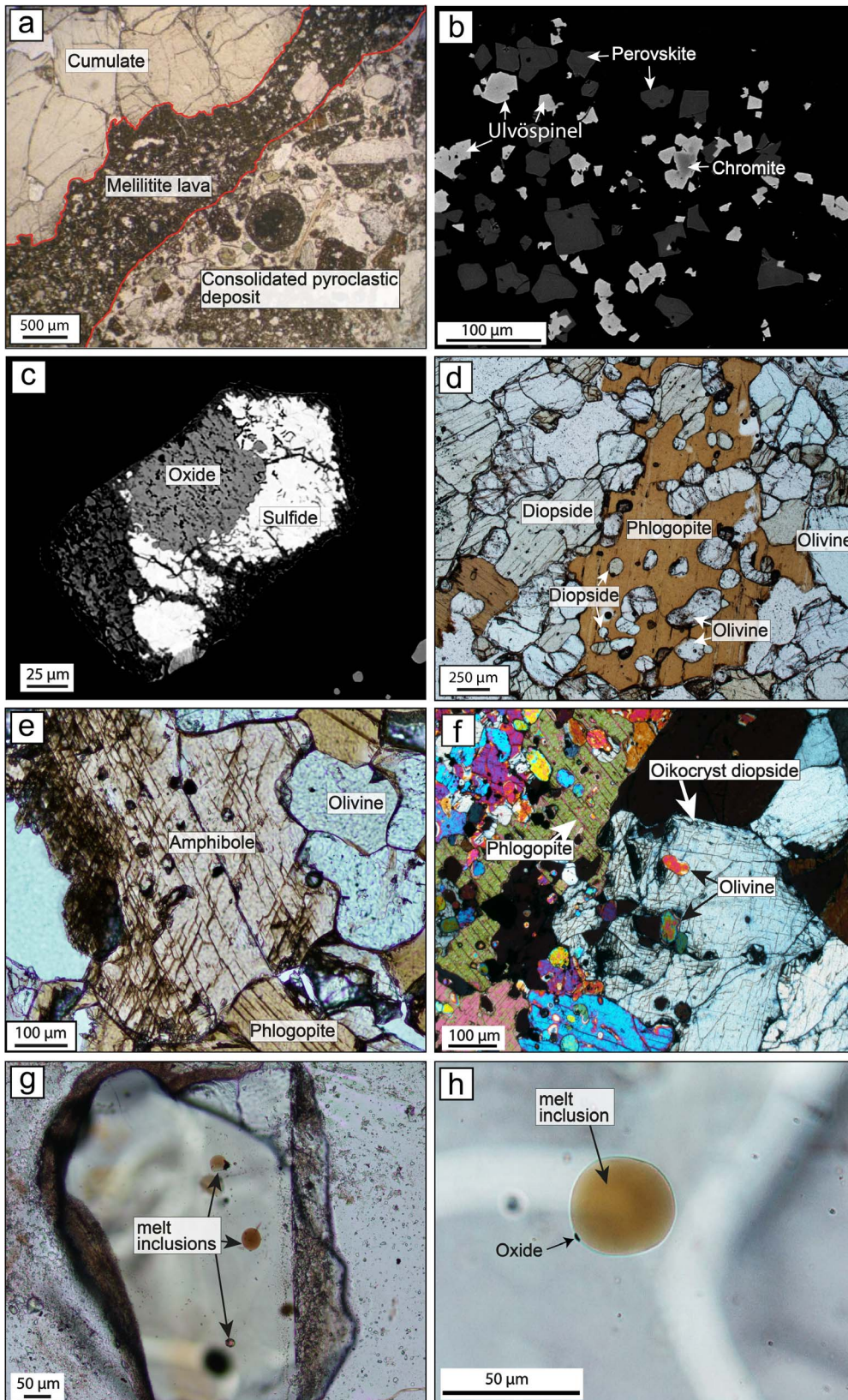


Fig. 2. Representative images of the petrographic textures and mineralogy in xenoliths. (a) Photomicrograph in plane-polarized light (PPL) displaying the association between cumulate, lava flow and the breccia area at the Embalulu Olatwa tuff ring. The drawn line delimits the cumulate part from the lava flow and the breccia; (b) BSE image of oxides in the lava surrounding sample 14TL22e; (c) Combination of xenomorphic oxide and sulfide observed in the lava carrying the Embalulu Olatwa xenoliths; (d) Photomicrograph in PPL of sample 14TL22b showing olivine, Cpx and phlogopite crystals (mineral assemblage observed in all xenoliths studied). Note the poikilitic fabric with phlogopite oikocrysts (2–4 mm) enclosing anhedral olivine chadacrysts; (e) Pargasite (amphibole) in combination with olivine and phlogopite from sample 14TL22a; (f) Cpx oikocryst enclosing olivine crystals in sample 14TL22e; (g) Olivine-hosted melt inclusions in sample 14TL22e; (h) High magnification photomicrograph of a melt inclusion from sample 14TL21.

with water to expose the MIs on the surface using aluminum disks. The sample was then cleaned ultrasonically, removed from the epoxy mounts and remounted in indium metal to minimize CO₂ and H₂O signal contamination by degassing under vacuum during secondary ion microprobe measurements. The indium mount was then stored at +60–80°C in a vacuum oven and coated with gold for the CO₂ and H₂O measurements. About 12 to 24 hours prior to analysis, the mount was placed into the sample storage chamber of the ion probe at ~10⁻⁸ Torr pressure. A liquid nitrogen cold trap and a sublimation pump were used to reduce CO₂ and H₂O background and maintain a pressure < 2 × 10⁻⁹ Torr in the sample chamber. The samples were sputtered with a ~0.1–0.8 nA, 10 kV ¹³³Cs⁺ primary beam focused to ~5 μm spot and then rastered to ~10×10 μm. A field aperture of ~1000 μm was used to eliminate secondary ion signal from the spot margins. A mass-resolving power of ~5000 was applied to resolve ¹⁷O on ¹⁶O¹H, ²⁹Si¹H on ³⁰Si, ³¹P¹H on ³²S and ³⁴S¹H on ³⁵Cl peaks. The energy slit was centered and opened to 40 eV. No energy offset was applied. The ¹²C⁻ (counting time 8 s), ¹⁷O²⁻ (3 s), ¹⁶OH⁻ (6 s), ¹⁸O²⁻ (3 s), ¹⁹F⁻ (4 s), ²⁷Al⁻ (3 s), ³⁰Si⁻ (3 s), ³²S⁻ (4 s) and ³⁵Cl⁻ (6 s) ions were counted after 300 s pre-sputtering during 10 cycles in mono-collection mode using the axial electron multiplier and FC2 Faraday cap detectors. The normal-incidence electron flood gun was used to compensate for the sample charge. A set of reference glasses (A99 USNM 113498/1, M34, M40, M43, M48) and San Carlos olivine were analyzed to establish calibration lines during each analytical session (see supplementary material Fig.S1) and used to determine volatile concentrations in the unknown samples. In addition to the laboratory basaltic standards, four additional reference materials, corresponding in major element composition to olivine nephelinite with various amounts of H₂O and CO₂ (MELI-4 to MELI-10; see below and supplementary spreadsheet for the major and volatile elements composition), were prepared at the Laboratoire Magmas et Volcans (Clermont-Ferrand, France). They were created to account for the known matrix composition effects occurring during volatile measurements by SIMS (Hauri et al., 2002). Based on the established calibration lines, the accuracy of SIMS analyses (calculated as average relative deviation of the measured values from the reference ones) is 1–30% for CO₂ (1–9% using olivine nephelinite standards only), 1–40% for H₂O (1–10% using olivine nephelinite standards only), 15–34% for F, 17–42% for S and 13–30% for Cl, varying between the two sessions.

Piston-cylinder experiments (SIMS standards preparation)

Volatile-bearing olivine nephelinite standards were synthesized using a 3/4" piston-cylinder apparatus (Clermont-Ferrand, France) in order to calibrate SIMS measurements. The starting material for the experiments was a synthetic, CO₂-bearing olivine nephelinite powder, in which CO₂ was incorporated as MgCO₃ (see supplementary material for details). On a volatile-free basis, the composition of the starting powder is similar to those measured in MIs. About 100 mg of this powder were loaded along with deionized water in Au₈₀-Pd₂₀ containers (5 mm outer diameter, 4.6 mm inner diameter), that were subsequently welded shut. Piston-cylinder experiments were performed at a pressure of 500 MPa, 750 MPa and 1 GPa and a temperature T = 1300°C (slightly above liquidus). After three hours, the experiments were quenched isobarically, and then slowly decompressed. Despite the relatively high quench rate of the piston-cylinder, pockets affected by the growth of dendritic or spherulitic crystals were almost systematically observed in the final glasses. Hydrogen and carbon in the nephelinitic

glasses were measured with a Thermo Scientific™ FLASH 2000 CHNS elemental analyzer and a Bruker Vertex 70 FTIR spectrometer, following the protocols described by Buso et al. (2022). The four new olivine nephelinite standards contain 0.32–2.69 wt % H₂O and 0.98–2.09 wt % CO₂ (see supplementary datasheet).

RESULTS

Petrography and microstructures of the xenoliths

The studied cumulate xenoliths have a mineral assemblage made of olivine (40–50 vol %; Fig. 2d–f; vol % estimated from EBSD maps of the thin sections, see Fig. 3a–b and supplementary Figs. S2 & S4), phlogopite (0.6–21.5 vol %; Fig. 2d–f), amphibole (0–27.5 vol %, pargasite; Fig. 2e), Cpx (21–48 vol %, diopside; Fig. 2d–f), and accessory minerals (titanomagnetite ~0.5 vol. %, pyrrhotite ~0.5 vol. %; Fig. 2c). One out of ~30 olivine subhedral grains contains rounded 30–200 μm MIs (Fig. 2g–h). Olivine-hosted MIs are of great interest as they may be considered to have been isolated from any interaction with external fluids and melt, or from alteration (Roedder, 1984; Frezzotti, 2001). The analyzed MIs are hosted in olivine crystals in samples 14TL21 and 14TL22e. The MIs are primary glassy inclusions (randomly distributed within the host olivine) with rare small oxides at the edge (up to 5 μm in diameter; Fig. 2h & Fig. S12). The MIs do not contain vapor bubble. Mineral assemblage similar to that observed in the xenoliths has been described in pyroxenites from the Natron area by Dawson & Smith (1992) with resorbed olivine (Fo_{73–83}), Cpx and phlogopite phenocrysts. Olivine-phlogopite micro-ijolites, that crystallized from phonolitic melts in the Oldoinyo Lengai volcanic system, have similar olivine (Fo_{79–85}) and phlogopite (Mg# = 84) compositions, but have more alkali-rich Cpx (diopside, aegirine or augite) and crystallized a groundmass made of nepheline, sulfides, titanite, apatite, wollastonite and Ti-andradite (Sekisova et al., 2015; Baudouin & France, 2019; Halász et al., 2023).

The texture and grain size highlight two populations of olivine grains: 1) large crystals of subhedral olivine (200–1400 μm; Fig. 2e & Fig. 3e), which represent 80% to 85% of total olivine grains in the samples, and 2) anhedral olivine chadacrysts (mostly 50–300 μm; Fig. 2d & Fig. 3e) that are enclosed in phlogopite (Fig. 2d) and Cpx oikocrysts (up to 1.5 mm; Fig. 2f & Fig. 3f). Subhedral olivine grains commonly form aggregates with 120° triple junctions, which are characteristic of equilibrated cumulate assemblages (Fig. 4). Phosphorus maps of olivine highlight that both types of olivine display fossils of initial skeletal growth, resorbed features following this initial stage, and subsequent P-poor olivine overgrowths (Fig. 4). Sample 14TL22b contains coarse (300–1200 μm) olivine and Cpx grains (Fig. 3e–f), as well as phlogopite oikocrysts enclosing small resorbed olivine chadacrysts (poikilitic texture; Fig. 2d). Sample 14TL22e is similar to sample 14TL22b with phlogopite and Cpx oikocrysts enclosing roundish olivine grains. Sample 14TL22e is delimited by a Cpx vein with large grains (up to 3 mm; see supplementary Figs. S4 & S5). Oxides and sulfides (<300 μm, mostly <100 μm) are euhedral when included in silicate phases and anhedral when interstitial. Locally, rounded Cpx chadacrysts are enclosed by phlogopite. Sample 14TL21 has relatively large olivine grains (in average 350 μm; Fig. 3e and supplementary Fig. S7), interstitial Cpx and phlogopite grains and a Cpx vein (Fig. 3a). Although larger grains (up to 500 μm) are present, oxides and sulfides are usually small (20–100 μm). Sample 14TL22a displays a grain-size layering (Fig. 3b). In an olivine-rich band, coarse-grained olivine is associated with fine-grained amphibole grains (Fig. 3b); this band is in contact with two finer grained bands. Larger xenomorphic amphibole grains (Fig. 2e) are locally

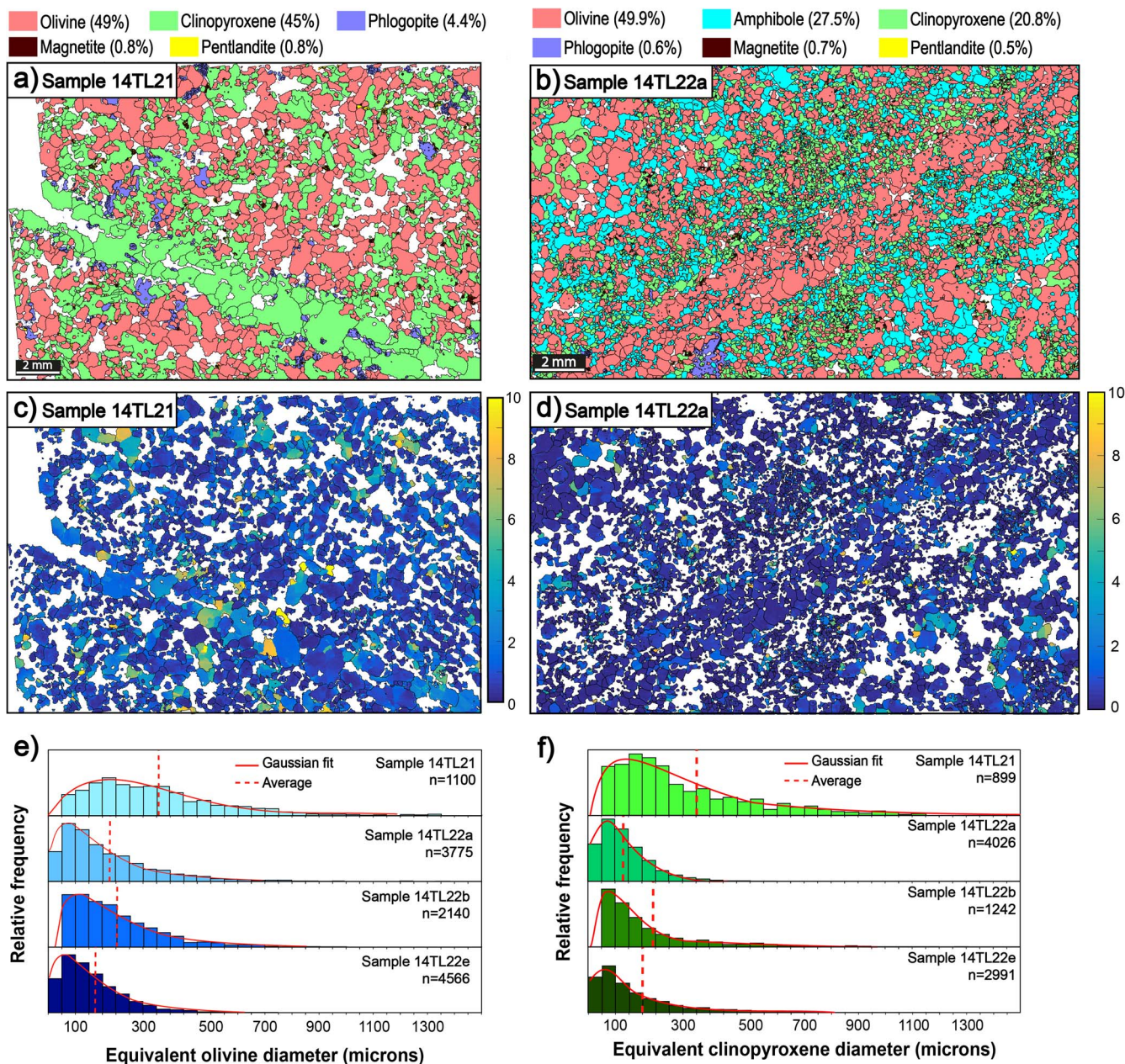


Fig. 3. EBSD processed maps representative of (a) and (c) sample 14TL21; (b) and (d) sample 14TL22a. (a-b) Phase maps where each color corresponds to a phase; (c-d) Maps of Mis2Mean in olivine and Cpx, with threshold of misorientation angle for grain boundaries set at 10°; (e) Equivalent diameter for olivine grains measured by EBSD. The solid curve represents a gaussian fit and the dashed line is the average for each sample; (f) Equivalent diameter for Cpx grains measured by EBSD.

highly altered. Olivine grain sizes in 14TL22a are on average smaller than those from the other studied xenoliths (Fig. 3e). Some rare phlogopite oikocrysts in sample 14TL22a enclose amphibole chadacrysts, showing that phlogopite crystallizes after amphibole. The association of phlogopite and amphibole was found only in sample 14TL22a where amphibole modal content is high (27%).

The studied samples show no clear microstructural evidence for deformation or magmatic layering (Fig. 3c-d and supplementary Figs. S2-S7). The CPOs are poorly defined, with no clear fabric and very low J-indexes for olivine and Cpx (J index <2; Fig. 5) in comparison with naturally-deformed peridotites documented in literature with J-index up to ~20 (Ismail & Mainprice, 1998; Tommasi et al., 2000). Phlogopite and Cpx grains have low GOS

values (<5), and low shape factors (<4), even for large oikocryst grains (Fig. 6). GOS and shape factor values for each sample are reported in Table 1.

Mineral major element compositions

The average major element concentrations of all minerals are presented in Table 2. Olivine in samples 14TL21, 14TL22b and 14TL22e displays homogeneous forsterite (Fo) contents (Fo = 100 × Mg/(Mg + Fe) in mol %) around Fo₈₁₋₈₂ (Fig. 7a), similar to Fo contents observed in olivine melilitite (in average ~Fo₈₂) or olivine nephelinite lavas (bimodal olivine compositions with Fo₅₂₋₆₅ and Fo₇₇₋₉₀) from the Natron region (Mattsson et al., 2013). Sample 14TL22a, with the highest molar fraction of amphibole (27 vol %; Fig. 3b), contains olivine with a significantly lower Fo

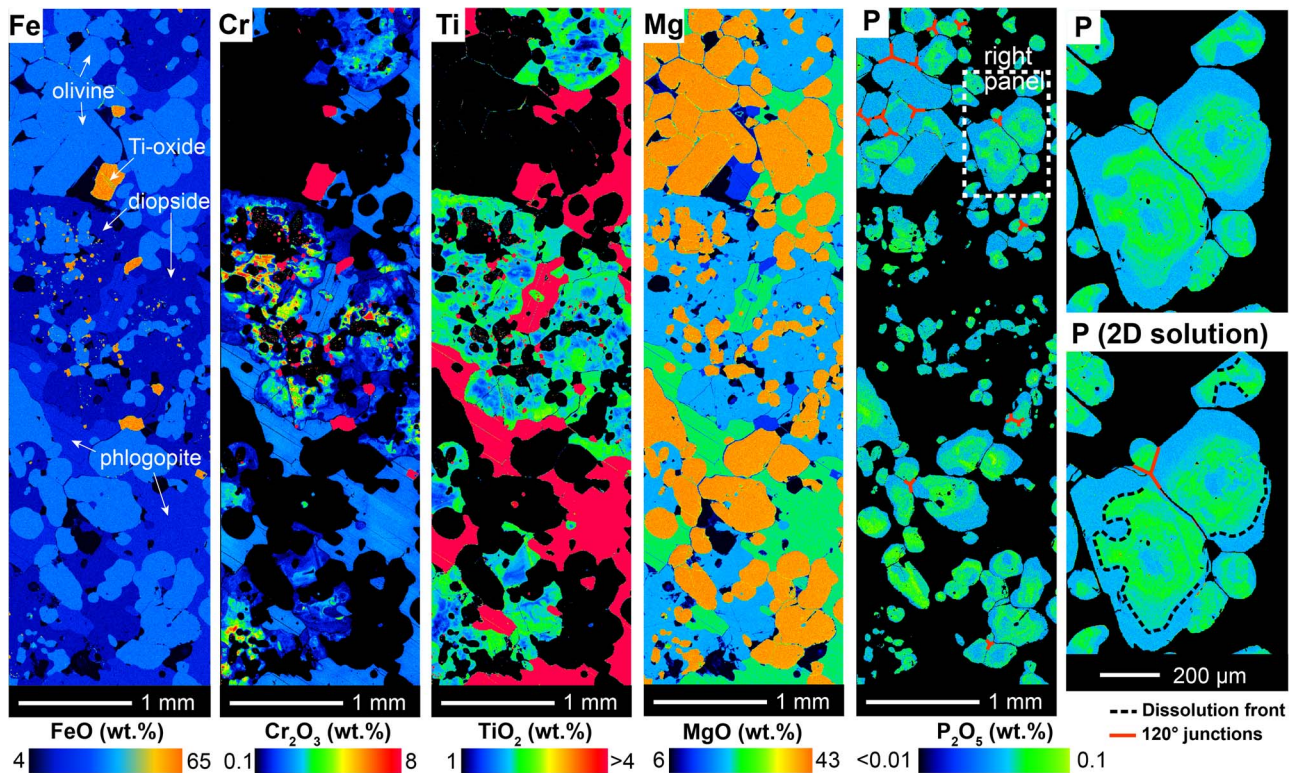


Fig. 4. X-ray maps (Fe, Cr, Ti, Mg, P) of Embalulu Oltatwa xenolith. Cores of diopside oikocrysts are enriched in Cr and depleted in Ti compared to their rims. Olivine grains do not have Mg zonation (and no Ca, Al zonation). The truncation in P in olivine suggests a dissolution event that separates the olivine core from its rim. Olivine grains preserve a dendritic framework, suggesting that olivine grains from the xenolith have a magmatic origin. Note that only olivine grains are displayed in the P map.

content ($\sim\text{Fo}_{78}$). Olivine from Embalulu Oltatwa xenoliths have lower Fo contents and higher Ca contents ($\sim 1500\text{--}2900$ ppm; Fig. 7a) compared to olivines derived from lithospheric mantle source (Fo > 90 and Ca < 1000 ppm), but similar Ca-content and Fo content as olivines from Oldoinyo Lengai olivine-phlogopite ijolites (Dawson & Smith, 1992; Dawson *et al.*, 1995; Sekisova *et al.*, 2015; Halász *et al.*, 2023), from primitive olivine from olivine nephelinite lavas (Fo₇₇₋₉₀; Mattsson *et al.*, 2013) or from melilitite lavas (Fo₈₀₋₉₀; Mattsson *et al.*, 2013).

The composition of pyroxenes (Wo₄₇₋₄₉En₄₃₋₄₅Fs₇₋₁₀) lies in the diopside compositional space. Major element concentrations in Cpx are similar from one sample to another in Al (0.6–3.2 wt % Al₂O₃), Ti (0.6–1.9 wt % TiO₂) and Na (0.5–0.9 wt. Na₂O). Diopside oikocrysts display complex zoning in Cr and Ti, with the crystal core enriched in Cr and depleted in Ti compared to their rim (Fig. 4). Diopside grains have no clear zoning in Ca, Fe, Mg, Na and Al. Mg# (Mg# = Mg/[Mg + Fe_{TOT}]) in diopside ranges from 82 to 86.5. Sample 14TL22a (amphibole-rich sample) displays the lowest Mg# (and Ca content) and highest Na contents of the sample series. Diopside grains from Embalulu Oltatwa have Na and Mg concentrations (in atoms per formula unit) similar to diopside from olivine-phlogopite micro-ijolites (Fig. 7b; Halász *et al.*, 2023) and overlap with diopside from melilitite lavas (Mattsson *et al.*, 2013), but lower Na contents than diopside from ijolites (Baudouin *et al.*, 2020) from Oldoinyo Lengai and higher Mg concentrations than diopside from olivine nephelinite lavas (Fig. 7b; Mattsson *et al.*, 2013). Micas present in the xenoliths are phlogopite (Mg# $\sim 80\text{--}81$, 4.3–4.8 wt % TiO₂; Fig. 7c). Their composition is similar to phlogopite from metasomatic veins in peridotites described by Dawson & Smith (1988), and also similar to phlogopite in melilitite and olivine nephelinite rocks

(Mattsson *et al.*, 2013), and olivine-phlogopite micro-ijolites (Halász *et al.*, 2023). Phlogopite grains from sample 14TL22a have K/Na values ~ 8 , which is significantly lower than phlogopite from the other xenoliths (K/Na ~ 12). The Mg# of phlogopite grains in sample 14TL22a (~ 81) is slightly lower than that of phlogopite grains from the other samples (Mg# = 81–84). Amphibole grains from sample 14TL22a are (Ti, K) pargasitic hornblende with 3–4 wt % TiO₂, 1.5 wt % K₂O and a Mg# of 80. Titanomagnetite or ulvöspinel compositional range is Usp₅₇₋₆₈Wu₂₂₋₄₁Mag₂₋₁₆ (Usp: ulvöspinel, Wu: wüstite; Mag: magnetite) with 58–66 wt % Fe_T, 15–18 wt % TiO₂, 3–8 wt % Cr₂O₃. Al, Mg and Cr decrease with decreasing Usp contents. Perovskite grains (only observed in the lava carrying the xenoliths; Fig. 2b) have 56–59 wt % TiO₂ and 38–40 wt % CaO. Chromite grains from the host lavas have ~ 32 wt % Cr₂O₃ and ~ 39 wt % FeO. Sulfides from the host lava are pentlandite or pyrrhotite.

Melt inclusions major element and volatile contents

The silicate glass in olivine-hosted MIs from the two samples have similar compositions with 15.6–15.9 wt % MgO (Mg# $\sim 75\text{--}81$; Table 2) before corrections for post-entrapment crystallization (PEC). The MIs are corrected for PEC and Fe-loss using the Petrolog3 software (Danyushevsky & Plechov, 2011). MIs major compositions are recalculated to equilibrium with the host olivine using the model from Danyushevsky (2001) that is calibrated for hydrous melt compositions (recalculated compositions and associated entrapment temperature are presented in Table 2). The olivine composition was calculated using $K_d^{\text{Fe-Mg}}$ defined by the model of Toplis (2005). The amount of total iron (Fe_T) is

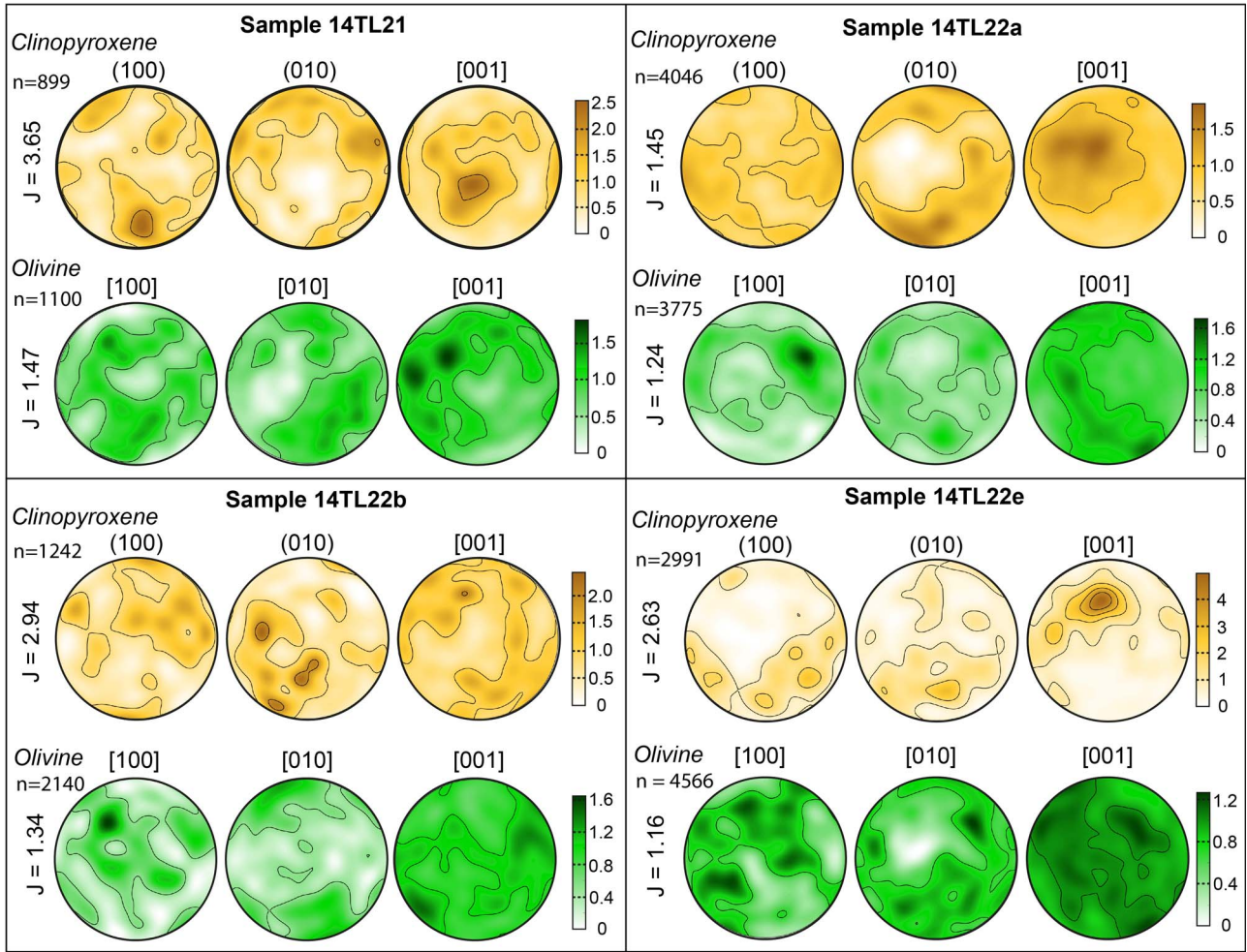


Fig. 5. Crystal preferred orientations (CPOs) of olivine and Cpx in the xenoliths from Embalulu Oltatwa (Oldoinyo Lengai). Using the J-index index, olivine and Cpx grains from the studied xenoliths have a random distribution. The studied samples show no clear microstructural evidence for deformation or magmatic layering. The number of indexed points and J-index for the mineral phases (olivine, Cpx, phlogopite) are reported in Table 2. Note that Cpx J-index in sample 14TL21 is probably overestimated because of the small number of indexed grains.

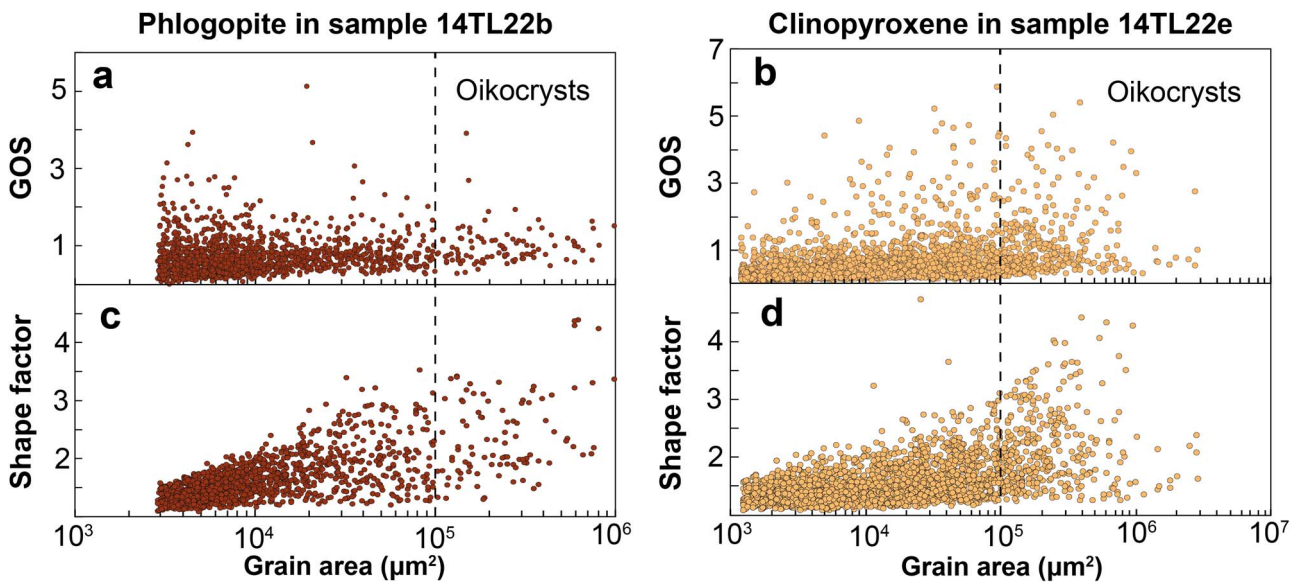


Fig. 6. Grain Orientation Spread (GOS) and shape factor of phlogopite in sample 14TL22b (a, c, e) and Cpx in sample 14TL22e (b, d, f). Variations of the parameters are similar in the four studied xenoliths, although here we report the details for two representative samples where most oikocrysts were observed. All parameters were obtained by grain analyses of the EBSD data. A threshold of grain area of $10^5 \mu\text{m}^2$ was set to distinguish fine-grained ($<10^5 \mu\text{m}^2$) from the coarse-grained (oikocrysts) counterparts.

Table 1: Electron Back Scattered Diffraction parameters and index values

Sample name		14TL21			14TL22a			14TL22b			14TL22e			
EBSD setup	Step size (μm)	25			15			23			15			
	Olivine	49			49.9			47.4			40.3			
Mineral modal %	Clinopyroxene	45.2			20.8			31.2			47.8			
	Phlogopite	4.3			0.6			21.3			9.5			
	Pargasite	0.1			27.5			0.1			0.1			
	Magnetite	0.8			0.7			0.1			1.2			
	Pentlandite	0.7			0.5			0.1			1.1			
	# grains	1100			3775			2140			4566			
	J-index	1.21			1.09			1.1			1.05			
M-index	0			0			0			0				
Olivine		Mean	Min	Max	Mean	Min	Max	Mean	Min	Max	Mean	Min	Max	
	Size (μm)	342	66	1512	198	40	1288	225	61	1480	157	40	1237	
	GOS	0.98	0.12	6.69	0.58	0.04	5.83	0.75	0.09	6.07	0.55	0.04	5.8	
	Axial ratio	1.51	1.02	5.05	1.49	1	14.27	1.48	1	4.51	1.42	1	4.29	
	Tortuosity	1.15	1	1.71	1.14	1	2.16	1.12	1	1.81	1.11	1	2.02	
	KAM	0.54	0	9.19	0.26	0	9.62	0.5	0	8.7	0.3	0	9.72	
	Shape factor	1.36	1.09	2.35	1.35	1.07	2.9	1.31	1.07	2.32	1.28	1.07	2.82	
	Mis2Mean	0.87	0	12.2	0.48	0	11.47	0.69	0	6.47	0.45	0	5.82	
			[100]	[010]	[001]	[100]	[010]	[001]	[100]	[010]	[001]	[100]	[010]	[001]
	Mean p _f -index	1.05	1.05	1.06	1.03	1.01	1.03	1.03	1.02	1.02	1.02	1.02	1.03	1.03
	# grains	899			4026			1242			2991			
	J-index	1.91			1.23			1.82			2.31			
	M-index	0.01			0.01			0.01			0.03			
Clinopyroxene		Mean	Min	Max	Mean	Min	Max	Mean	Min	Max	Mean	Min	Max	
	Size (μm)	329	66	2258	132	40	940	214	61	1520	180	40	1926	
	GOS	1.13	0.17	6.1	0.43	0.06	10.45	1.08	0.08	5.9	0.61	0.07	5.89	
	Axial ratio	1.6	1.01	5.02	1.51	1	4.94	1.61	1	5.25	1.83	1	22.76	
	Tortuosity	1.17	1	2.06	1.12	1	2.12	1.16	1	2.54	1.2	1	2.82	
	KAM	0.57	0	9.8	0.28	0	9.41	0.69	0	9.43	0.35	0	9.29	
	Shape factor	1.44	1.09	3.16	1.34	1.07	3.16	1.43	1.09	3.97	1.55	1.08	4.72	
	Mis2Mean	0.99	0	7.76	0.37	0	8.12	1.12	0	8.39	0.68	0	10.41	
			(100)	(010)	[001]	(100)	(010)	[001]	(100)	(010)	[001]	(100)	(010)	[001]
	Mean p _f -index	1.13	1.14	1.16	1.02	1.08	1.07	1.09	1.14	1.08	1.31	1.18	1.5	
	# grains	429			130			1833			1480			
	J-index	4.83			10.04			3.72			23.04			
	M-index	0.02			0.04			0.05			0.11			
Phlogopite		Mean	Min	Max	Mean	Min	Max	Mean	Min	Max	Mean	Min	Max	
	Size (μm)	140	67	1028	97	40	1009	135	61	1123	102	40	1331	
	GOS	1.04	0.07	5.13	0.5	0.03	2.7	0.66	0	5.12	0.56	0.06	4.8	
	Axial ratio	1.71	1.02	6.73	1.84	1.04	11.02	1.69	1.01	16.69	1.73	1.01	5.31	
	Tortuosity	1.17	1	2.15	1.2	1.01	2.38	1.22	1	3.09	1.22	1	3.09	
	KAM	0.87	0	9.92	0.65	0	7.45	0.65	0	8.96	0.52	0	8.63	
	Shape factor	1.49	1.1	3.46	1.56	1.12	3.41	1.59	1.08	4.39	1.62	1.09	5.21	
	Mis2Mean	1.15	0	9.57	0.95	0	8.58	0.79	0	7.97	0.77	0	9.09	

estimated from the olivine nephelinite average whole-rock composition from the Natron lake magmatic province (~15 wt %; [Mattsson et al., 2013](#)). Petrolog3 corrections were done at a fixed oxygen fugacity ($f\text{O}_2$) of FMQ=0 (where FMQ stands for Fayalite Quartz Magnetite redox buffer; additional calculations using the FMQ +1.5 redox state are presented in the supplementary material). PEC corrections required from 0.7 to 18% olivine addition to the MIs composition to achieve equilibrium with the host crystal.

The average MgO content of MIs after PEC correction is ~7.5 to 9.5 wt % MgO, which is below MgO values for the most primitive olivine nephelinites in the region (~17 wt % MgO; [Mattsson et al., 2013](#)) and suggests that olivine nephelinitic melts supplying the

Embalulu Oltatwa vent underwent olivine (and potentially oxides) crystallization before the entrapment of the MIs. The lower MgO value after PEC correction is likely related to the consideration of iron loss from MI by Petrolog3 models. Nevertheless, comparison with olivine nephelinite lavas from the Natron lake magmatic province should be conducted with great caution as those contain large amounts of phenocrysts and accessory minerals that likely significantly skew the bulk-rock composition, and eventually does not represent melt composition. The variability in SiO_2 (39–43.5 wt %; [Fig. 8a](#)), and MgO (~7.5–9.5 wt % after corrections for PEC) in the MIs can be explained by olivine fractionation. The classification of [Le Bas \(1989\)](#) places them in the field of olivine nephelinites ([Fig. 8b](#)) with $\text{SiO}_2 + \text{Al}_2\text{O}_3 \sim 50.6\text{--}54.7$ wt %, and

Table 2: Average major element composition of minerals observed in Embalulu Oltatwa xenoliths (Oldoinyo Lengai)

Olivine	n*	SiO₂	Al₂O₃	TiO₂	CaO	Na₂O	K₂O	MnO	MgO	FeO	Cr₂O₃	NiO	P₂O₅	Total	Fo	
Sample 14TL21	18	39.58	0.01	0.02	0.31	0.02	b.l.d	0.26	42.86	17.02	0.02	0.28	0.01	100.4	81.8	
±2σ		1.09	0.02	0.03	0.04	0.03	0.01	0.06	0.38	0.67	0.03	0.10	0.03			
Sample 14TL22a	19	39.35	0.02	0.01	0.26	0.03	b.l.d	0.36	40.32	20.30	0.01	0.26	0.01	101.0	78.0	
±2σ		0.50	0.10	0.02	0.03	0.03	0.01	0.07	0.33	0.43	0.02	0.15	0.05			
Sample 14TL22b	12	39.99	0.05	0.02	0.30	0.03	0.01	0.27	42.57	17.83	0.00	0.08	0.00	101.1	81.0	
±2σ		0.49	0.23	0.02	0.03	0.03	0.01	0.08	0.75	0.96	0.02	0.17	0.02			
Sample 14TL22e	37	39.35	0.00	0.02	0.32	0.02	0.01	0.28	42.44	17.27	0.01	0.16	0.02	99.9	81.4	
±2σ		0.84	0.02	0.05	0.07	0.02	0.02	0.12	0.77	0.81	0.04	0.13	0.04			
Clinopyroxene	n	SiO₂	Al₂O₃	TiO₂	CaO	Na₂O	K₂O	MnO	MgO	FeO	Cr₂O₃	NiO	P₂O₅	Total	Mg#	
Sample 14TL21	18	51.66	2.07	1.34	23.17	0.69	0.01	0.07	15.22	5.14	0.30	0.03	0.34	100.0	84.1	
±2σ		1.63	0.61	0.42	0.36	0.13	0.02	0.14	0.48	0.48	0.26	0.10	0.06			
Sample 14TL22a	18	52.90	1.60	1.08	22.82	0.84	0.01	0.08	15.13	5.54	0.21	0.03	0.33	100.6	83.0	
±2σ		0.84	0.37	0.16	0.28	0.07	0.02	0.08	0.15	0.28	0.11	0.08	0.06			
Sample 14TL22b	9	52.49	1.90	1.29	23.38	0.63	b.l.d	0.11	15.46	4.58	0.43	0.04	0.36	100.7	85.8	
±2σ		0.80	0.86	0.34	0.14	0.06	0.01	0.07	0.36	0.35	0.31	0.06	0.05			
Sample 14TL22e	16	51.53	2.29	1.18	23.26	0.70	0.01	0.08	15.05	5.07	0.28	0.02	0.34	99.8	84.1	
±2σ		0.67	0.37	0.51	0.43	0.10	0.02	0.07	0.22	0.36	0.24	0.04	0.06			
Phlogopite	n	SiO₂	Al₂O₃	TiO₂	CaO	Na₂O	K₂O	MnO	MgO	FeO	Cr₂O₃	NiO	P₂O₅	Total		
Sample 14TL21	10	37.99	14.38	4.60	b.l.d	0.73	9.48	0.04	19.83	7.68	0.45	0.13	b.l.d	95.3		
±2σ		0.99	0.23	0.12	0.00	0.05	0.10	0.04	0.23	0.26	0.04	0.08	0.01			
Sample 14TL22a	3	38.51	14.04	4.40	b.l.d	1.15	8.90	0.07	19.64	8.60	0.17	0.13	0.01	95.6		
±2σ		0.36	0.17	0.09	0.01	0.02	0.08	0.06	0.35	0.04	0.01	0.07	0.02			
Sample 14TL22b	11	38.21	14.17	4.57	b.l.d	0.78	9.57	0.03	19.82	7.62	0.52	0.08	b.l.d	95.4		
±2σ		0.63	0.20	0.08	0.02	0.07	0.15	0.04	0.53	0.33	0.16	0.08	0.01			
Sample 14TL22e	11	37.49	14.40	4.51	0.01	0.83	9.11	0.04	19.76	8.01	0.45	0.11	0.01	94.7		
±2σ		0.67	0.43	0.26	0.02	0.08	1.28	0.05	0.23	0.47	0.06	0.07	0.03			
Amphibole	n	SiO₂	Al₂O₃	TiO₂	CaO	Na₂O	K₂O	MnO	MgO	FeO	Cr₂O₃	NiO	P₂O₅	Total		
Sample 14TL22a	25	43.49	9.98	3.76	11.46	2.82	1.52	0.07	15.85	8.47	0.37	0.07	0.17	98.0		
±2σ		0.75	0.56	0.20	0.19	0.11	0.10	0.07	0.28	0.46	0.21	0.07	0.04			
Oxide	n	SiO₂	Al₂O₃	TiO₂	CaO	Na₂O	K₂O	MnO	MgO	FeO	Cr₂O₃	NiO	P₂O₅	Total		
Sample 14TL21	7	0.29	3.17	17.21	0.02	0.03	b.l.d	0.36	7.94	59.97	6.85	0.33	b.l.d	96.2		
±2σ		0.45	0.80	0.82	0.02	0.04	0.01	0.09	0.07	1.08	0.33	0.10	0.00			
Sample 14TL22a	10	0.14	3.05	17.19	0.04	0.01	0.01	0.41	6.24	64.59	3.45	0.32	b.l.d	95.4		
±2σ		0.36	0.43	0.27	0.03	0.02	0.01	0.07	0.12	1.05	0.08	0.13	0.00			
Sample 14TL22b	1	0.13	3.12	17.65	0.08	0.01	0.03	0.35	7.85	60.48	6.64	0.03	b.l.d	96.4		
Sample 14TL22e	3	0.00	3.98	15.91	0.02	b.l.d	b.l.d	0.40	7.62	61.53	7.36	0.22	b.l.d	97.0		
±2σ		0.01	0.13	0.03	0.02	0.01	0.01	0.05	0.09	0.11	0.04	0.04	0.00			
Melt inclusion	n	SiO₂	Al₂O₃	TiO₂	CaO	Na₂O	K₂O	MnO	MgO	FeO_t	Cr₂O₃	P₂O₅	NiO	SO₃	Cl	Total
Sample 14TL21	18	40.77	10.28	4.31	11.91	2.23	2.13	0.08	15.87	7.48	0.57	0.19	0.11	0.06	0.02	95.9
±2σ		1.15	0.35	0.34	0.22	0.30	0.30	0.03	0.46	0.32	0.11	0.07	0.07	0.04	0.01	
Sample 14TL22e	94	41.83	10.54	3.85	11.83	2.43	1.69	0.10	15.70	7.52	0.51	0.19	0.08	0.06	0.03	96.3
±2σ		0.87	0.54	0.31	0.21	0.28	0.39	0.05	0.66	0.36	0.09	0.05	0.06	0.04	0.04	
Post-entrapment corrected inclusions	n	SiO₂	Al₂O₃	TiO₂	CaO	Na₂O	K₂O	MnO	MgO	Fe₂O₃	Fe₂O	Cr₂O₃	P₂O₅	T(°C)	Mg#	Total
Sample 14TL21	18	40.51	11.36	4.76	13.20	2.47	2.40	0.06	7.83	3.53	11.82	0.63	0.20	1127	81.8	100.0
±2σ		1.50	0.74	0.68	0.99	0.56	0.57	0.07	1.24	1.20	1.07	0.20	0.11	46	0.9	
Sample 14TL22e	94	41.49	11.44	4.19	12.87	2.64	1.84	0.08	8.10	3.06	12.24	0.56	0.20	1134	81.3	100.0
±2σ		1.30	1.03	0.61	0.67	0.50	0.60	0.10	1.19	0.70	0.62	0.17	0.10	40	1.3	

CaO + Na₂O + K₂O ~ 15.8 to 20 wt % and Mg# ~ 49–57 (Fig. 8c). Those are named olivine nephelinites herein to mark their difference with the alkaline nephelinites that represent in the area highly evolved magmas.

The trapping temperature of the MIs (estimated with the Petrolog3 software using the olivine-melt thermometer of Beattie, 1993) is 1127 ± 46°C for sample 14TL21 and 1134 ± 40°C for sample 14TL22e. One hundred and twenty-five MIs have been measured

to quantify their volatile contents (see supplementary datasheet for volatile compositions of individual MIs). They have variable CO₂ contents (up to 6074 ppm; Fig. 9a), and 0.9 to 1.5 wt % H₂O (5 MIs have <0.5 wt % H₂O). The CO₂ content in MIs is not reconstructed as no inclusion presents vapor bubbles.

The S concentrations of MIs range from ~20 to 130 ppm (Fig. 9b). These low values are consistent with the presence of sulfides in the samples. MIs have been screened for sulfides,

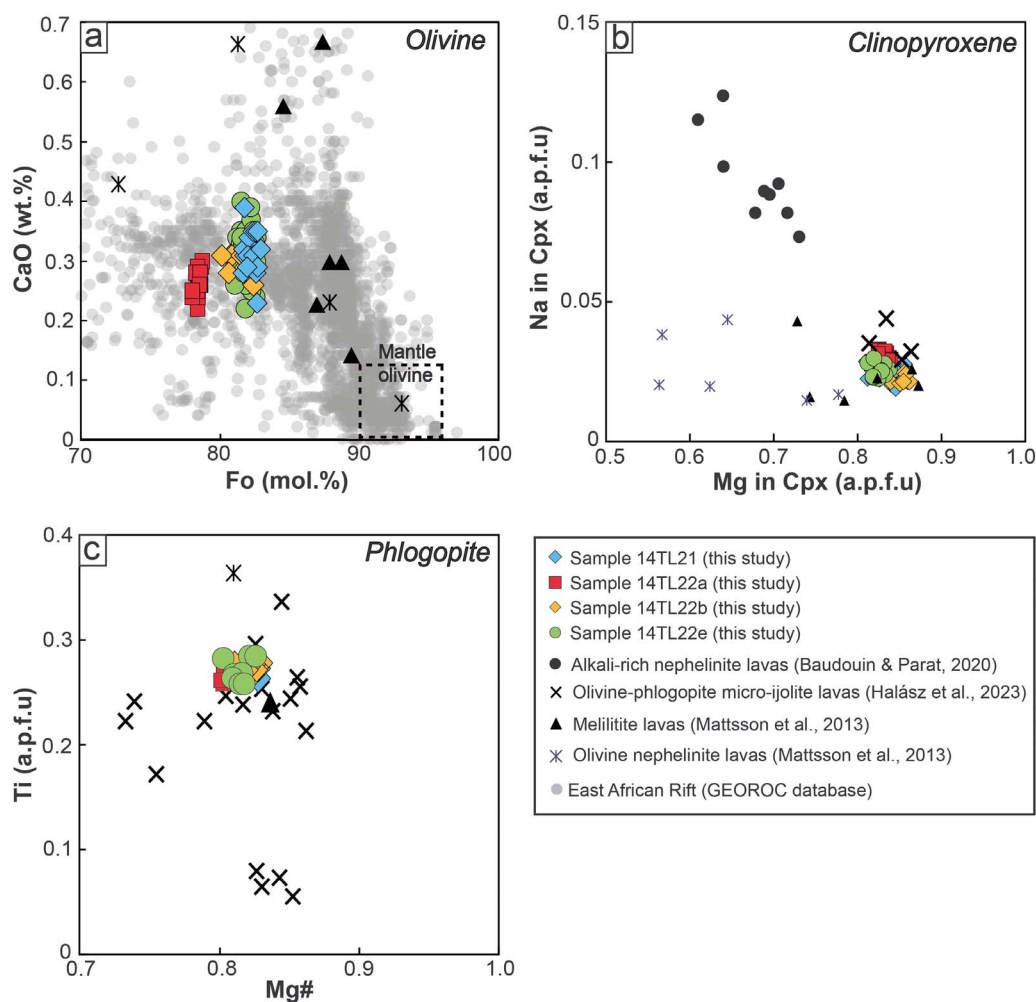


Fig. 7. (a) CaO contents vs. Fo (Fo = Mg/[Mg + Fe]) contents of olivine from Embalulu Oltatwa xenoliths. The dotted box represents the field for olivines derived from lithospheric mantle source (Halász et al., 2023). East African Rift olivine data are from the GEOROC database (<https://georoc.mpch-mainz.gwdg.de/georoc>); (b) Na (in atoms per formula unit: a.p.f.u.) vs. Mg (a.p.f.u.) in diopside from alkali-rich nephelinite (Baudouin & Parat, 2020), olivine-phlogopite micro-ijolite (Halász et al., 2023) and olivine nephelinite (this study) from Oldoinyo Lengai; (c) Ti (a.p.f.u.) – Mg# diagram for phlogopites (crosses are phlogopite data from olivine-phlogopite micro-ijolite from Oldoinyo Lengai; Halász et al., 2023).

but most MIs do not present large sulfides. Corrections related to sulfide restorations lead to large uncertainties. Therefore, S concentrations reported here are minimum values that are not corrected. There is no apparent correlation between S concentration and K_2O , H_2O , or CO_2 concentrations.

The abundance of Cl in MIs ranges from ~50 to 540 ppm (Fig. 9c). The concentration of Cl increases slightly with increasing F (Fig. 9c). However, Cl concentration is not correlated with H_2O or CO_2 concentration. The concentration of F varies from ~390 to 4500 ppm, with the two highest F concentrations measured in sample 14TL21. S/Cl ratios range from 0.14 to 1.21 (Fig. 9d) and are negatively correlated with the F concentrations.

Trace element compositions

Olivine

Olivine crystals in the four xenoliths have highly variable rare earth element (REE) concentrations, from LREE-poor grains to variably LREE-enriched grains (Fig. 10a). Measured olivine grains were selected for their clearness and absence of visible micro-inclusions, and laser pits were placed away from cracks and grain boundaries; therefore, we report strongly constrained LREE enrichments. Olivine grains displaying enrichments in REE are also enriched in HFSE (Zr, Nb, Ta, Hf) and LILE (Rb, Ba, Th, U,

Eu) elements in comparison to LREE-poor grains (Fig. 10b). HREE contents are more homogeneous and vary from 0.15 to 0.53 times the chondrite value. LREE enrichments can be quantified by the $(La/Sm)_N$ and $(La/Lu)_N$ ratios (with the subscript 'N' for the normalization to chondrite values). $(La/Sm)_N$ varies from 0.19 to 2.6, and $(La/Lu)_N$ varies from 0.06 to 16.7 in olivine grains.

Clinopyroxene

We analyzed the concentrations of trace elements in diopside using at least 9 crystals from each xenolith, differentiating between Cpx oikocrysts and Cpx grains composing recrystallized veins. No significant difference has been identified in trace elements between core and rim analyses, and between the various petrological types (background assemblage, oikocryst, veins; Fig. 10c–d). Similarly to major elements, trace elements document more evolved compositions for sample 14TL22a that displays the highest incompatible element concentrations (Fig. 10c–d). More generally, REE contents and element relative fractionations (e.g. La/Sm, Sm/Yb) are relatively similar between the various samples with relatively flat patterns from LREE to MREE with $(La/Sm)_N = 0.75–0.93$ and depletion in HREE with $(Sm/Yb)_N = 7.4–11.6$. All samples show a typical Zr negative anomaly ($Zr^* = 0.4–0.6$ with $Zr^* = 2 \times Zr_n / (Nd_n + Hf_n)$).

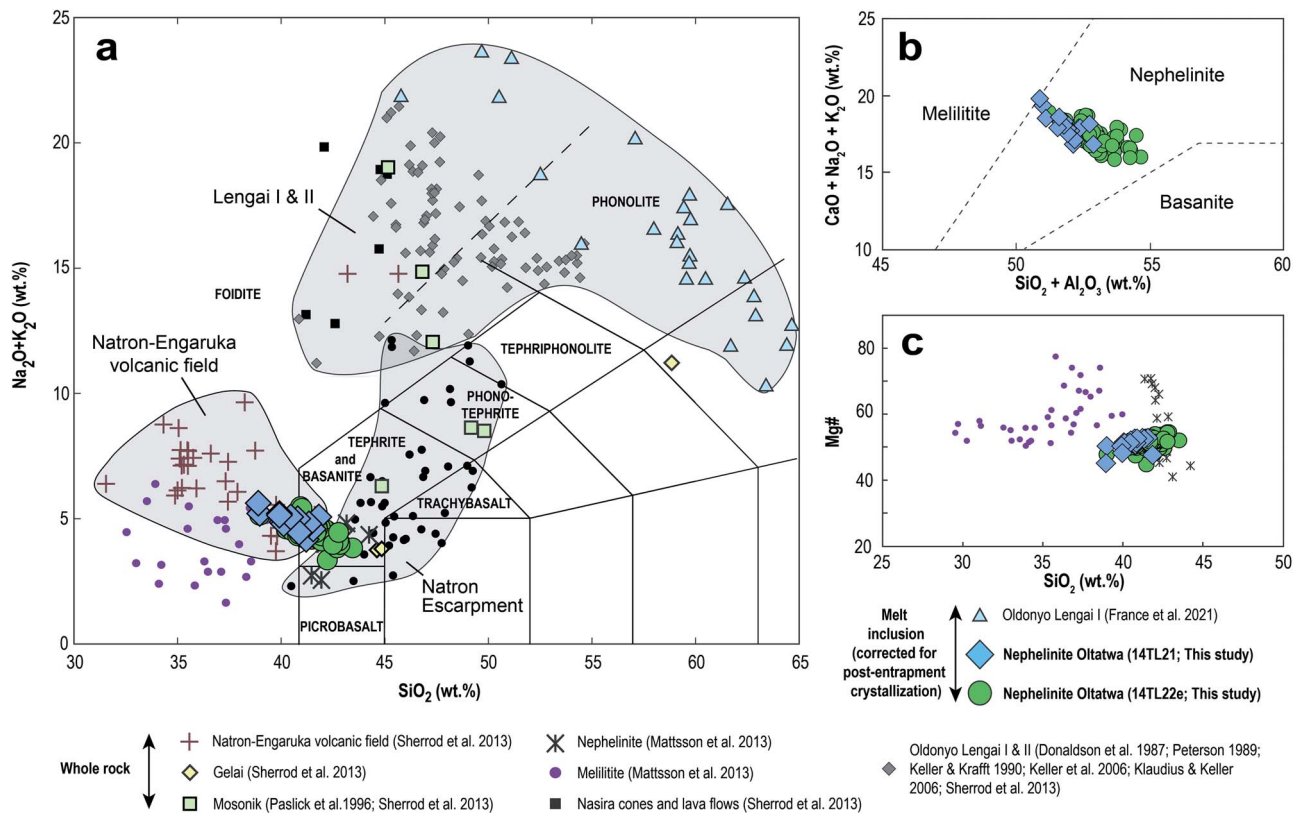


Fig. 8. Geochemical classification of olivine-hosted melt inclusions from Embalulu Olatwa crater. (a) Alkali vs. silica composition; (b) Nephelinite–melilitite–basanite classification of *Le Bas* (1989). Melt inclusions from olivine crystals have a nephelinitic composition; (c) SiO_2 versus Mg# of melt inclusions compared with whole-rock olivine nephelinites and melilitites from *Mattsson et al.* (2013).

DISCUSSION

The studied xenoliths document the igneous processes that govern the evolution of relatively primitive melts in a continental rift setting, and more specifically in a carbonatite province. Hereafter, we estimate the composition of parental melts, including their volatile content, of olivine nephelinitic cumulates and provide evidence for reactive porous flow in deep crustal mushy magma reservoirs beneath the Oldoinyo Lengai volcano. Then, we discuss the solidification path of the cumulative assemblages and the evolution of associated melts in relation with the Natron lake igneous province.

A lower crust reservoir beneath the Oldoinyo Lengai volcano

Geophysical investigations and petrological constraints highlight that the mid/upper crust reservoir is both filled and recharged by relatively evolved melts and that the differentiation stage that produces alkaline nephelinite should occur at deeper levels, potentially within the lower crust mushy reservoir (Albaric et al., 2010; Bosshard-Stadlin et al., 2014; Roecker et al., 2017; Weinstein et al., 2017; Reiss et al., 2021). The cumulates studied herein, that crystallized from relatively primitive olivine nephelinite melts, likely formed in those deeper levels. The absence of volatile bubbles in MIs strongly suggests that volatile saturation was not reached while MIs were entrapped, thus highlighting that the estimated entrapment pressure is a minimum estimate for melt entrapment, thus consistent with crystallization within the active deep crustal mushy reservoir.

Major and trace element composition of cumulates' parental melts in the Oldoinyo Lengai volcanic system

MIs have 7.5 to 9.5 wt % MgO after correction for PEC (up to ~16 wt % MgO before PEC corrections), which is the most primitive melts directly observed at Oldoinyo Lengai, but are likely more evolved than the most primitive olivine nephelinites in the Natron region (~17 wt % MgO; *Mattsson et al.*, 2013), whose compositions may be affected by their important crystal cargo load. The variability in the $\text{K}_2\text{O}/\text{Na}_2\text{O}$ ratio (0.26–1.89) in MIs advocates for slightly different mafic magma batches with different K_2O contents that crystallized olivine. We estimate the REE composition of the silicate melts in equilibrium with Cpx using the major element composition of Cpx grains and the prediction of trace element partitioning between Cpx and melt is a function of pressure (P), temperature (T) and Cpx composition (*Wood & Blundy*, 1997). Trace element partitioning between Cpx and melt is a function of pressure (P), temperature (T) and Cpx composition (*Wood & Blundy*, 1997). For the trace element Cpx/melt partition coefficients calculations, we fixed $T = 1100^\circ\text{C}$ and $P = 300$ MPa or 1 GPa (similar to lower crustal depths). The REE composition of silicate melts in equilibrium with Cpx is relatively similar to the whole-rock composition of olivine nephelinite lavas from the Natron province (*Fig. 11*; *Mattsson et al.*, 2013) and supports that Cpx crystallized from silicate melt with a composition close to the whole-rock composition of olivine nephelinite lavas.

Volatile content of olivine nephelinite melts

We constrain the volatile concentrations of the least evolved melts of the Oldoinyo Lengai igneous system by using the volatile composition of olivine-hosted MIs related to olivine nephelinite

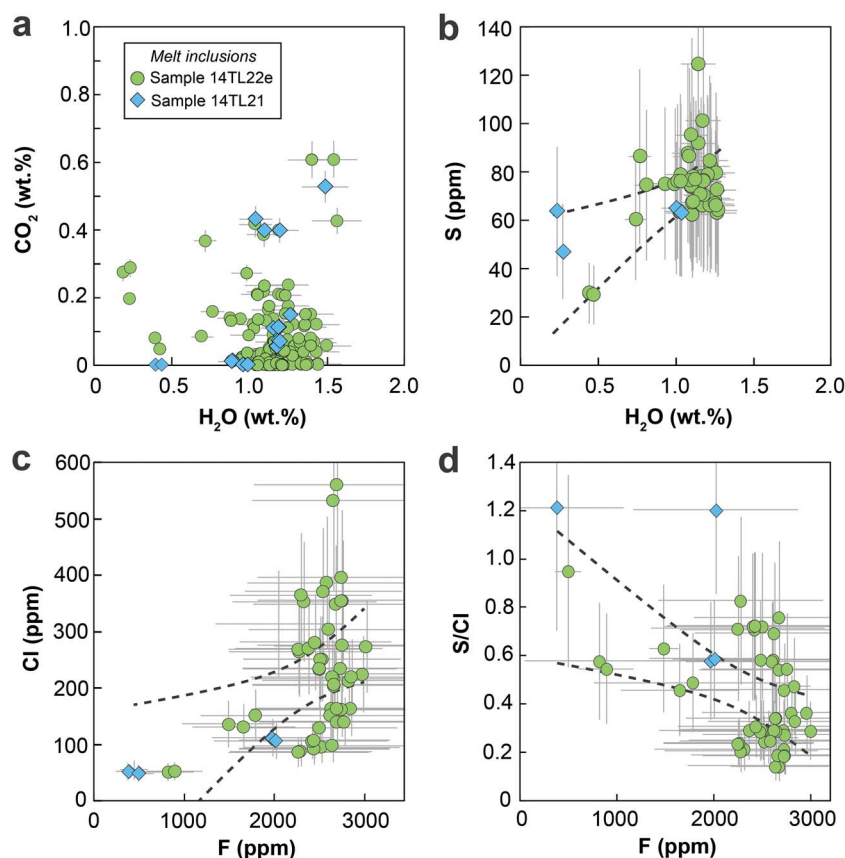


Fig. 9. Volatile concentrations in olivine-hosted MIs from Embalulu Oltatwa xenoliths. (a) H_2O vs. CO_2 contents. H_2O were not reconstructed for the potential H loss, therefore, H_2O concentrations measured in the melt inclusions are minimum values. CO_2 contents were not reconstructed for the formation of vapor bubbles (e.g. Wallace *et al.*, 2015) since none of the measured inclusion displayed vapor bubble; (b) H_2O vs. S contents; (c) F vs. Cl contents. Overall, melt inclusions from sample 14TL22e display the highest Cl and S contents; (d) F vs. S/Cl contents. 99% confidence intervals on the regression are shown with dashed lines.

magmas. Olivine nephelinite melts from the present study have higher H_2O content (up to 1.5 wt % H_2O) than those from relatively similar olivine nephelinite lavas from Kwaraha and Labait, two volcanoes located ~200 km to the South (0.2–0.5 wt % H_2O ; Baudouin & Parat, 2020). This difference in water content cannot be explained by magma differentiation as more than 60% of fractional crystallization would be required to account for such an increase (considering H_2O as perfectly incompatible), a degree of fractionation at odds with the primitive major element composition of the studied MIs. Alternatively, a lower degree of melting at Oldoinyo Lengai (compared to Kwaraha and Labait) would also explain higher H_2O contents in melts. Nevertheless, previous authors (Mattsson *et al.*, 2013; Baudouin & Parat, 2020) have shown that degrees of mantle partial melting are similar between Oldoinyo Lengai area and Southern edifices (Kwaraha, Labait), ruling out the latter hypothesis. We propose that the lithospheric mantle source beneath the Oldoinyo Lengai is likely more hydrated than the mantle feeding other volcanoes from the North Tanzanian Divergence (i.e. Kwaraha, Labait). This is consistent with the strong metasomatic overprint at Oldoinyo Lengai with hydrous minerals like phlogopite (Dawson & Smith, 1988). H_2O - CO_2 concentrations in MIs overlap with those measured at Nyiragongo and Nyamulagira volcanoes in the Western branch of the East African Rift (up to 1.5 wt % H_2O , up to 14000 ppm CO_2 ; Connors *et al.*, 2020). MIs are poor in sulfur (~20 to 130 ppm). S concentrations are lower than in MORB glasses (~800–1500 ppm; Métrich & Wallace, 2008), OIB (up to ~3000 ppm; e.g. ~1100 ppm S

in pre-eruptive melts of Kilauea's 2018 eruption; Lerner *et al.*, 2021) or arc settings (~1000–3000 ppm; Métrich & Wallace, 2008). The low sulfur concentration can be explained by various processes (source, differentiation). First, olivine nephelinites might be significantly sulfide-undersaturated due to low sulfur contents in the mantle source. Second, significant amounts of sulfides may have crystallized before MIs entrapment (sulfides are present in the cumulative assemblages). Alternatively, similarly to what have been reported for water (e.g. Gaetani *et al.*, 2012; Bucholz *et al.*, 2013), sulfur concentrations potentially re-equilibrated through the host olivine crystal by diffusion, and would, therefore, document the interstitial melt S composition that likely account for sulfides crystallization after MI entrapment. S concentrations measured in MIs are, therefore, minimum values for the olivine nephelinite S concentrations. To constrain the amount of S potentially degassed from the melt, we modeled the sulfur content at sulfide saturation (SCSS^{2-}), which is the amount of sulfur that can be dissolved in a melt before an immiscible sulfide phase is exsolved (Fig. 12a–b). We compared three SCSS^{2-} models (Smythe *et al.*, 2017; O'Neill, 2021; Li & Zhang, 2022) using the PySulfSat tool (Wieser & Gleeson, 2022). We considered two sulfide composition end-members with molar $\text{Fe}/(\text{Fe} + \text{Cu} + \text{Ni})$ or $a_{\text{FeS}} = 0.5$ and $a_{\text{FeS}} = 1$, and maintain the sulfide composition for all temperatures (Fig. 12a–b). Pressure is assumed to be 1 GPa and H_2O content is assumed to be 1.2 – H_2O . MIs have degassed between 400 and 800 ppm S depending on the SCSS^{2-} model if $a_{\text{FeS}} = 0.5$ (25% to 90% of the S pre-eruptive budget) and between

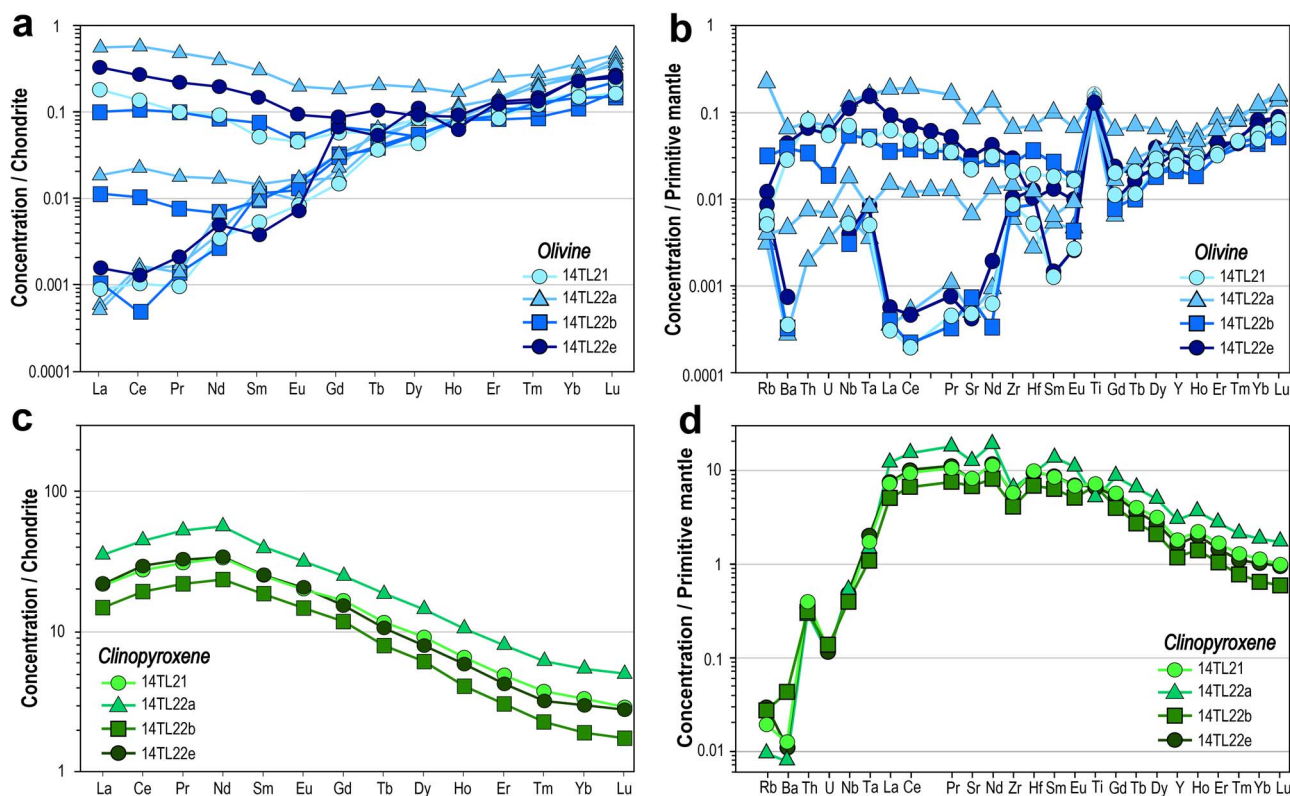


Fig. 10. Representative analyses of trace elements compositional variations in olivine and Cpx. (a-b) Olivine. (a) chondrite-normalized Rare Earth Element (REE) concentrations and (b) primitive mantle-normalized trace element concentration; (c-d) Cpx; (c) Chondrite-normalized REE concentrations; (d) Primitive mantle-normalized trace element concentrations. Chondrite values and primitive mantle values from [McDonough & Sun \(1995\)](#).

900–2000 ppm S if $a_{\text{FeS}} = 1$ (>90% of the S pre-eruptive budget). However, highly degassed S in MIs is at odds with the higher solubility of S compared to CO_2 ([Métrich & Wallace, 2008](#)) at depths (and the fact that MIs have high CO_2 concentrations). Therefore, we propose that S concentrations in MIs potentially document further crystallization of sulfides in interstitial melt after MIs entrapment, and a potential reequilibration through diffusion of sulfur in MIs with this interstitial melt (like observed experimentally for water). This process has not been reported yet to our knowledge and may be explored further experimentally.

Cl concentrations in MIs vary from ~50 to 540 ppm. These values are higher than the pre-eruptive concentrations of unaltered MORB (<100 ppm; [Jambon et al., 1995](#)) and OIB (<100 ppm; [Métrich & Wallace, 2008](#)) but are in the range of Cl concentrations measured in arc magmas (up to 7500 ppm; [Aiuppa et al., 2009](#)). Cl concentrations above 100 ppm are found in some MORB glasses that have high Cl/K values as a result of assimilation of hydrothermally altered materials ([France et al., 2014](#); [Fischer et al., 2016](#); [Marschall et al., 2017](#)) or directly of seawater (e.g. [Zhang et al., 2017](#)). There is, however, no evidence of any hydrothermal alteration in our samples or direct interaction with seawater. On the other hand, high Cl contents are also reported in the enriched mantle components (e.g. EM & HIMU; [Stronck & Haase, 2004](#)). They were ascribed either to devolatilization of subducted sedimentary material (EM components), or to recycled altered oceanic components in the lithosphere (HIMU), or to both. Mantle source of the Oldoinyo Lengai igneous series appears to be strongly metasomatized (e.g. [Dawson & Smith, 1988](#)) and has isotopic signatures of both EM1 and HIMU mantle components ([Keller et al., 2006](#); [Bell & Simonetti, 2010](#)). Thus, the high Cl

contents in the studied MIs are likely produced by a Cl-rich mantle source. Cl concentrations in MIs overlap with those measured by XRF in high-Mg olivine melilitite (whole-rock) from Oldoinyo Lengai (500 ± 180 ppm Cl; [Mangler et al., 2014](#)), but are much lower than the concentrations of Cl measured in highly differentiated magmas like natrocarbonatite (up to 59 300 ppm; [Mangler et al., 2014](#)), phonolites (2700 ± 650 ppm Cl; [Mangler et al., 2014](#)) and alkali-rich nephelinites from Oldoinyo Lengai (4650 ± 470 ppm Cl; [Mangler et al., 2014](#)).

F concentrations in MIs range from ~390 to 4500 ppm, which is greater than the pre-eruptive concentrations in unaltered MORB samples (100–600 ppm; [Jambon et al., 1995](#)), OIB (100–600 ppm; [Métrich & Wallace, 2008](#)) and arc magmas (~500 ppm; [Aiuppa et al., 2009](#)). F concentrations in MIs are similar to those measured in olivine melilitite lavas (whole-rocks with 2500 ± 300 ppm F; [Mangler et al., 2014](#)) and lower than those in highly differentiated magmas like natrocarbonatite (1.2–3.6 wt %; [Mangler et al., 2014](#)) from Oldoinyo Lengai. Moreover, the F/Cl values in MIs (~5–27) are higher than those in whole-rock high-Mg olivine melilitites (5 ± 1.9 ; [Mangler et al., 2014](#)). Both Cl and F are incompatible elements, but Cl has a more pronounced incompatibility during magmatic differentiation ([Pyle & Mather, 2009](#)). The Oldoinyo Lengai phonolites and natrocarbonatites typically have low F/Cl values (<1; [Mangler et al., 2014](#)) that were interpreted in favor of apatite fractionation in evolved melts (preferential decrease in F compared to Cl; [Mangler et al., 2014](#)). Therefore, high F/Cl values in MIs are interpreted as volatile concentrations in primitive melts before crystal fractionation.

The absence of volatile bubbles suggests that MIs were CO_2 undersaturated, making the estimation of entrapment pressure

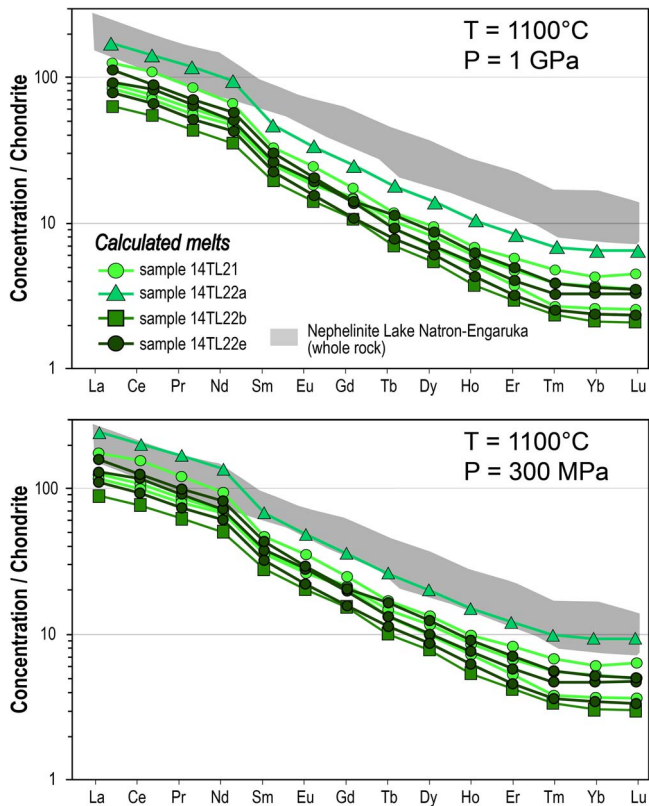


Fig. 11. Chondrite-normalized REE concentrations in Cpx. Chondrite values and primitive mantle values from McDonough & Sun (1995). The dark grey field is the reported whole rock composition of nephelinite from Lake Natron-Engaruka (Mattsson et al., 2013). Melts are calculated from Cpx compositions and partition coefficients estimated from Wood & Blundy (1997) at $T = 1100^{\circ}\text{C}$ and $P = 300\text{ MPa}$ and 1 GPa and compared to whole-rock composition of nephelinite.

challenging. CO_2 solubility highly depends on the ratio of non-bridging oxygens to tetrahedrally coordinated anions (Brooker et al., 2001; $\text{NBO}/T \sim 1\text{--}1.3$ for olivine nephelinites). For the MI major element composition, we estimate the maximum amount of CO_2 that can be dissolved in the melt at 1 GPa to range from 4 to 6 wt % CO_2 , consistent with the undersaturated character of the studied MIs. The pressures at which a $\text{CO}_2\text{--H}_2\text{O}$ fluid would be saturated for each MI were calculated with the Iacono-Marziano (Iacono-Marziano et al., 2012), VolatileCalc (Dixon, 1997; Newman & Lowenstern, 2002), Shishkina (Shishkina et al., 2014) and MagmaSat (Ghiorso & Gualda, 2015) models, using v.1.0.1 of the VESCal package (Iacovino et al., 2021). The $\text{Fe}^{3+}/\text{Fe}_T$ ratio was assumed to be 0.15 in all MIs. The calculated saturation pressure associated with the studied MI is $\sim 300\text{ MPa}$ (Figure 12c–d) and corresponds to minimum entrapment pressures due to the CO_2 -undersaturated character of the MIs. The major element composition of the MIs can affect the calculated saturation pressure by almost a factor of 2 (Iacovino et al., 2021). The calculated isobars depend highly on the $\text{H}_2\text{O}\text{--}\text{CO}_2$ solubility model (Dixon, 1997; Newman & Lowenstern, 2002; Iacono-Marziano et al., 2012; Shishkina et al., 2014; Ghiorso & Gualda, 2015), but none of these models is perfectly calibrated for olivine nephelinites (see supplementary material), and entrapment pressure estimates should, therefore, be considered with caution. Minimum saturation pressures translate into depths up to 12 km (assuming a crustal density of $2900\text{ kg}\cdot\text{m}^{-3}$; Fig. 12d), corresponding to minimum entrapment

pressures for the MIs. Those depths ($>12\text{ km}$) are in agreement with the existence of a mushy reservoir in the lower crust (Reiss et al., 2021).

Notwithstanding the CO_2 undersaturated character of the studied MIs, we observe scatters in CO_2 and H_2O contents. Some of the processes explaining the scatter are magma mixing or assimilation (e.g. Atlas et al., 2006; Johnson et al., 2008), ascent-driven diffusive water loss (Rasmussen et al., 2017), MI decrepitation (MacLennan, 2017), pre-eruptive vertical convection (Wallace et al., 2015), CO_2 flushing (Blundy et al., 2010; Caricchi et al., 2018). CO_2 flushing and ascent-driven diffusive water loss seem unlikely processes to explain the scatter since the magma is H_2O - and CO_2 -undersaturated. Decrepitation of the MIs could explain low CO_2 values but none of the MIs display textural evidence of decrepitation. H_2O diffusive reequilibration with the interstitial melt is a function of the fraction of melt in the cumulate and the distance between the MIs and the interstitial melt. Thus, volatile heterogeneity in the MIs could be related to the H_2O diffusive reequilibration.

Initial skeletal olivine growth, cumulate formation and reactive porous flow in lower crustal mushes

We take advantage of concentration changes in slow diffusing elements like phosphorus (P) in olivine to get insights into the initial olivine growth of the xenoliths (Milman-Barris et al., 2008). Coarse and fine olivine grains have surfaces delineating areas of P-rich lamellae and areas of P-poor olivine overgrowth (Fig. 4). These features are interpreted as an initial skeletal growth of the olivine grains followed by dissolution (e.g. Milman-Barris et al., 2008; Welsch et al., 2014; Xing et al., 2017; Mourey et al., 2023). Both anhedral olivine chadacrysts enclosed in diopside and phlogopite oikocrysts, and euhedral coarse olivine grains have an initial skeletal growth, suggesting that all olivine grains formed in a magmatic reservoir and are not inherited mantle xenocrysts. This interpretation is also supported by the sparse deformation features (misorientation in grains) and weak CPO (Figs. 3 & 5), and by the Fo content of olivine ($\sim 78\text{--}82$) that is significantly lower than lithospheric mantle olivines (Fig. 7a). The initial skeletal growth implies a thermal and/or compositional disequilibrium triggering an undercooling stage (Faure et al., 2003; Mourey & Shea, 2019; Lang et al., 2021; Wallace et al., 2021; Shea et al., 2022). Olivine is the first phase to crystallize in the olivine nephelinite series, and a delay in nucleation may occur when a new melt is injected as the nucleation energy should be overcome. Olivine would thus start to crystallize at a temperature slightly lower than its liquidus temperature corresponding to undercooling crystallization, and thus to the formation of skeletal to dendritic crystals (Fig. 13a; Faure et al., 2003; Mourey & Shea, 2019; Wallace et al., 2021; Lang et al., 2021). Phosphorus partition coefficient being likely increased during fast olivine growth, it results that skeletal and dendritic crystals display P-rich zonations (Shea et al., 2019). After this stage of delayed nucleation and fast crystal growth, olivine texture can gradually mature toward polyhedral shapes (Fig. 13a), in association with lower P-incorporation in olivine (Shea et al., 2019). Resorption features and successive growth highlight that this stage of textural maturation was likely associated with successive magma recharges, reinjections, or with a reactive porous flow (Fig. 13a). A maturation stage of the olivine-rich cumulative assemblage is evidenced by the numerous 120° triple junction angles between olivine grains that attest of the former stabilization of a dunitic assemblage (Figs. 4 & 13).

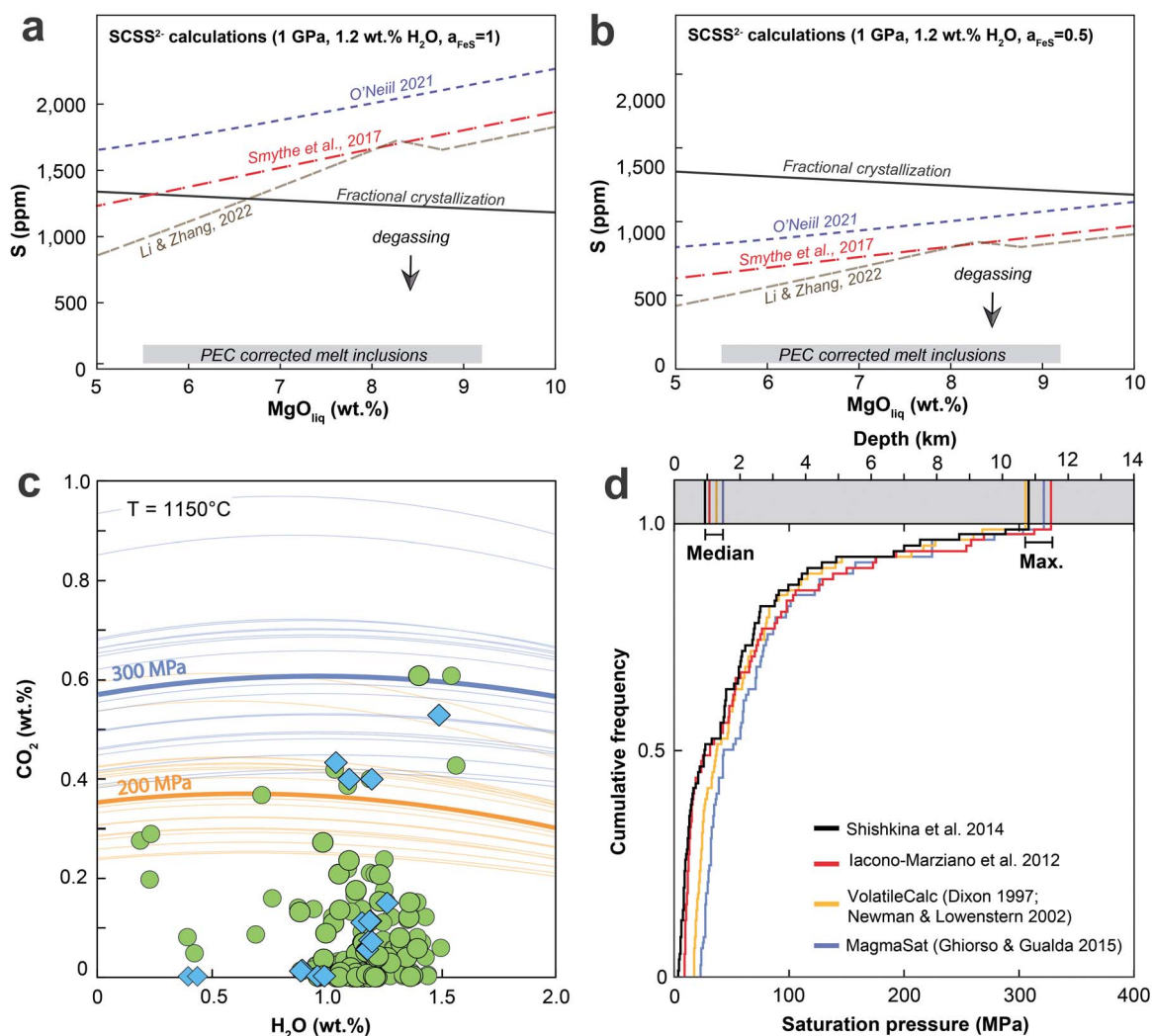


Fig. 12. (a-b) Sulfide saturation models using PySulfSat (Wieser & Gleeson, 2022). SCSS²⁻ model from Li & Zhang (2022) is H₂O sensitive unlike O'Neill (2021) and Smythe et al. (2017) models. Fractional crystallization path is calculated with S considered as an incompatible element. PEC-corrected melt inclusions are highly degassed in sulfur. (a) SCSS²⁻ with a sulfide composition of Fe/(Fe + Ni + Cu) or $a_{\text{FeS}} = 1$; (b) SCSS²⁻ with a sulfide composition of $a_{\text{FeS}} = 0.5$. Modeling SCSS²⁻ with a sulfide composition of $a_{\text{FeS}} = 0.5$ decreases the SCSS²⁻ by 45% compared to $a_{\text{FeS}} = 1$; (c) Saturation isobars for all melt inclusions from the samples (200 MPa and 300 MPa isobars) were computed at the specified pressure using VESical (v.1.0.1; Iacono et al., 2021) with the MagmaSat model (Ghiorso & Gualda, 2015) at 1150°C. The 200 and 300 MPa isobars are calculated for the major element composition of each individual melt inclusion (underlain as light curves, with the average isobar in bold). The 300 MPa isobars calculated from the composition of each MI overlap some of the H₂O-CO₂ space that is bracketed by the 200 MPa isobar calculated in MagmaSat. Note that the calculated saturation pressure corresponds to minimum entrapment pressures due to the CO₂-undersaturated character of the MIs; (d) Cumulative distribution functions of saturation pressures from different models for the studied melt inclusions. Fe³⁺/Fe_T was set to 0.15.

Based on MIs trapping temperature, olivine crystallization occurs at 1040–1170°C. Nevertheless, this temperature estimate may be considered with caution because of the initial delay in nucleation experienced by olivine, which could have skewed its composition. The grain size gradient with a subpopulation of smaller olivine grains in contact with an olivine/amphibole vein in sample 14TL22a (Fig. 3b) could be related to a recrystallization process of olivine grain where grain boundaries are locally displaced when temperature increases or flow stress decreases. Coarse and fine olivine grains from all samples have low shape factors (<3; Table 1), consistent with smooth grain boundaries (Ferrando et al., 2021a). Dissolution features in olivine grain chadacrysts (Figs. 2d & 4) suggest intense melt-rock interactions or reactive porous flows in which resorbed anhedral olivine chadacrysts acted as a nucleus to generate diopside and phlogopite oikocrysts (e.g. Halász et al., 2023). Anhedral olivine

chadacrysts enclosed in Cpx have been previously observed in olivine-phlogopite ijolites from Oldoinyo Lengai (Dawson et al., 1995; Sekisova et al., 2015; Halász et al., 2023) and interpreted as dissolution features following the injection of an olivine nephelinitic melt. We explain enrichments in LREE recorded in olivine (Fig. 10a) by a chromatographic effect at olivine grain boundaries through melt-rock interactions operating during a porous flow episode (Fig. 13b). The composition of the percolating liquid is not constrained but we suggest that the LREE content of the residual melt progressively increased during percolation, and the decrease of melt fraction (Fig. 13b). The similar major element composition in MIs from samples 14TL21 and 14TL22e advocates for a re-equilibration of major elements (and H₂O) after MIs entrapment. H₂O diffusion through host olivine and related reequilibration with the outer melt has been shown to proceed on tens of hours timescale, and volatile contents of melt inclusions

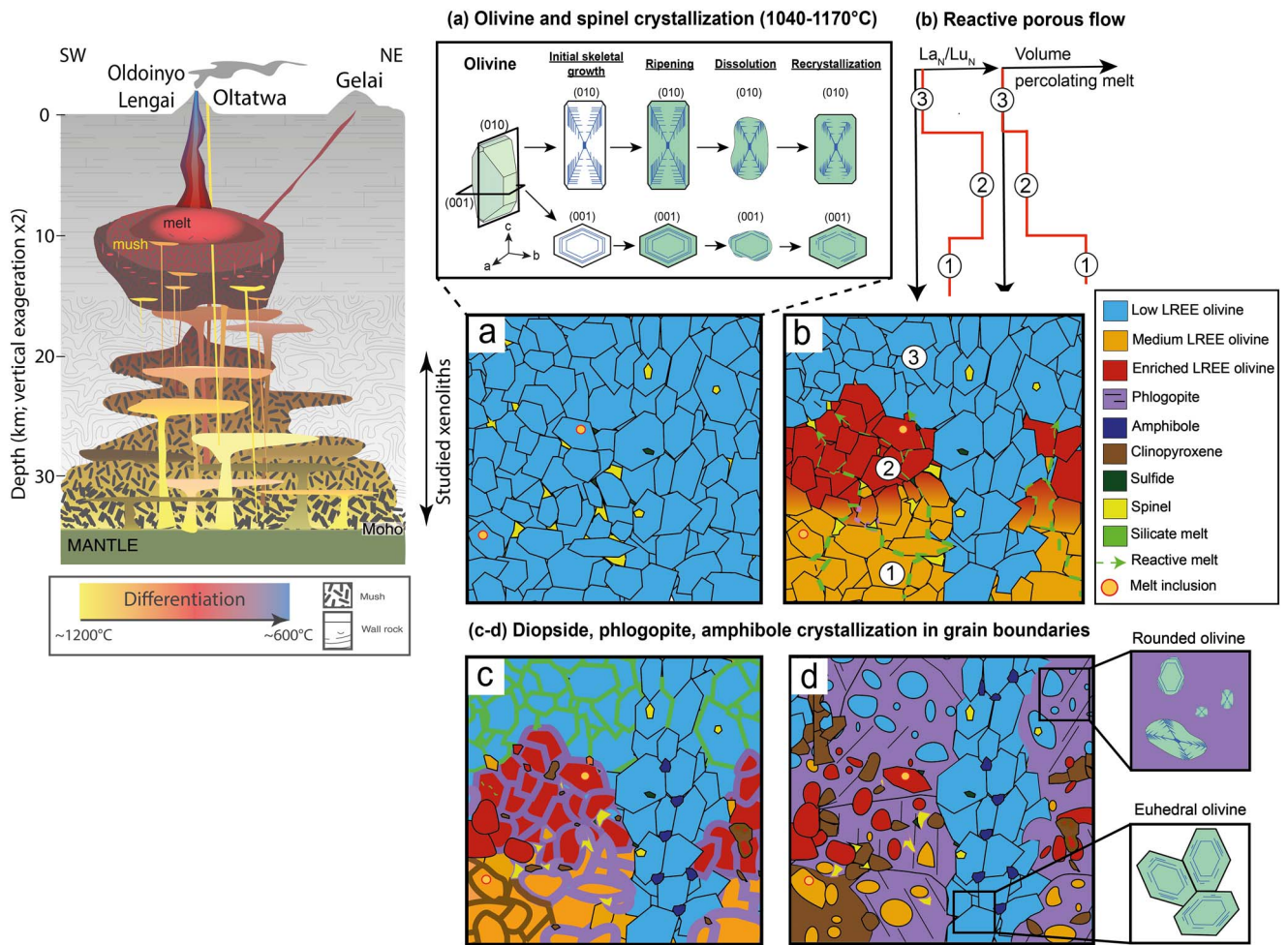


Fig. 13. Schematic evolution of the xenoliths during crystallization and melt-rock interactions at Oldoinyo Lengai in a conceptual transcrustal magmatic system inspired from [Cashman et al. \(2017\)](#), where deep relatively primitive mantle melts feed Embalulu Olatwa melts, and are transferred to mid- and finally upper crustal level reservoirs to produce phonolite and natrocarbonatite lavas. Vertical exaggeration is x2 (e.g. ~25 km of distance between Lengai & Gelai volcanoes). The Moho depth (~35 km) is from [Clutier et al. \(2021\)](#), and the presence of deep crustal mushes (~25 ± 5 km below the surface) from [Plasman et al. \(2017\)](#), [Roecker et al. \(2017\)](#), [Weinstein et al. \(2017\)](#). These mushes likely regularly feed mid- to upper-crust reservoir(s) that is located at depths of ~6 to 12 km ([Weinstein et al., 2017](#); [Reiss et al., 2021](#)). This shallower reservoir was recharged in 2007, triggering the 2007–2008 sub-Plinian eruption at Oldoinyo Lengai ([Albaric et al., 2010](#); [Bosshard-Stadlin et al., 2014](#)). It is also connected to the surface through a complex mushy plumbing system composed of interconnected dikes and sills ([Reiss et al., 2021](#)). (a) Olivine grains crystallize in a primitive melt with 7–10 wt % MgO at >320 MPa (>12 km below the surface). Inset in panel (a) highlight the initial skeletal olivine growth (P-rich lamellae), crystal ripening, dissolution and re-crystallization; (b) A reactive porous flow occurs after the percolation of a silicate melt in grain boundaries. LREE elements (highly incompatible in olivine) are progressively incorporated in olivine grains; (c) Cpx and phlogopite crystallize during magma ascent at lower temperature (<1100°C); (d) Phlogopite and Cpx interstitial growth form a poikilitic texture where most olivine grains are embayed in interstitial phases. Olivine resorption creates a population of smaller grains (50–150 μm) observed in sample 14TL22a (slightly more evolved). Insets show the triple junctions for olivine euhedral grains (with their P enrichments) and rounded grains enclosed in phlogopite oikocrysts.

are thus usually quantified on quickly quenched pyroclastic deposits (e.g. [Gaetani et al., 2012](#); [Bucholz et al., 2013](#)). Here as cumulative-plutonic rocks are considered, the MI water contents likely documents the volatile content of the percolative melt that crystallized the minerals surrounding olivine (mainly Cpx and phlogopite). Cumulates' xenoliths were then recently brought to the surface quickly ([Mattsson, 2012](#)), and we assume that this stage did not affect their volatile content. Melt-rock interactions, like those observed in the xenoliths studied herein and locally acting in a reactive porous flow, are widespread in various igneous systems: in the oceanic crust (e.g. [Lissenberg & Dick, 2008](#); [Boulanger et al., 2020](#); [Boulanger et al., 2021](#); [Ferrando et al., 2021b](#); [Boulanger & France, 2023](#)) and related mantle sections ([Basch et al., 2018](#)), in the lower- and mid-arc crust ([Bouilhol et al., 2015](#);

[Cooper et al., 2016](#)), in the ocean island systems ([Gleeson et al., 2021](#)), or the large igneous provinces ([Zhu et al., 2023](#)). The widespread implication of melt-rock reactions in magma differentiation series makes such a process a central one in igneous petrology.

Previous studies focusing on olivine-phlogopite ijolites lavas from the Oldoinyo Lengai ([Halász et al., 2023](#)) showed that diopside crystallizes between 970 and 1070°C. The high CaO/Al₂O₃ values from 0.9–1.24 in MIs suggest that MIs do not record Cpx fractionation. We hypothesize that diopside oikocrysts ([Fig. 2f](#)) crystallized at temperatures slightly lower than those estimated for olivine (<1100°C). As demonstrated above, the studied xenoliths are magmatic products and not fragments of a metasomatized peridotite from the upper mantle. Alternatively, phlogopite and

diopside cumulates are already present in a shallow reservoir and are picked up during the ascent as it is explained for olivine-phlogopite ijolites from Oldoinyo Lengai (Halász et al., 2023). The presence of hydrous phases (phlogopite and amphibole; 1.6 to 2.1 wt % H₂O in phlogopite from Manyara-Balangida rift nephelinite lavas, Tanzania; Baudouin & Parat, 2020) in the xenoliths suggests that olivine nephelinites melts were H₂O-bearing when phlogopite and amphibole crystallized. MIs with up to 1.5 wt % H₂O advocate for H₂O-rich primitive melts at early stages of differentiation beneath Oldoinyo Lengai. In detail, sample 14TL22a contains diopside chadacrysts in phlogopite oikocrysts (Fig. 3b) with K/Na values in phlogopite from sample 14TL22a lower than K/Na values from the other xenoliths. Lower K/Na ratios in phlogopite from sample 14TL22a could indicate further fractional crystallization of phlogopite (Arai, 1986) and a possible reaction in a more evolved liquid (i.e. diopside + melt = pargasite + phlogopite).

Evolution of primitive olivine nephelinite melts; a petrogenetic link with evolved alkaline melts from the Natron province

Primitive magmas feeding Oldoinyo Lengai are silica-undersaturated and categorized into two main sub-groups: the olivine melilitites and olivine nephelinites (Mattsson et al., 2013; Weidendorfer et al., 2019; Berkesi et al., 2023). Olivine melilitites are characterized by high Mg# (up to 0.75; Mattsson et al., 2013), high Ni (up to 0.46 wt %) and Cr contents (100–600 ppm; Keller et al., 2006), and the presence of Cpx, olivine, melilite, phlogopite, perovskite phenocrysts, nepheline and Ti-garnet microphenocrysts (Mattsson et al., 2013). In olivine nephelinite lavas, Cpx, olivine phenocrysts and spinel microphenocrysts are present but phlogopite and perovskite are usually absent. The absence of phlogopite in the olivine nephelinite lavas suggests that phlogopite oikocrysts in our xenoliths crystallized at a stage slightly more evolved (lower melt fraction) than the stage corresponding to the extraction of erupted olivine nephelinites. The variability of Mg# in the olivine melilitites is explained by variable degrees of olivine fractional crystallization in the lavas (Mattsson et al., 2013).

Olivine nephelinites and olivine melilitites are primitive melts that can form, at Oldoinyo Lengai, phonolitic and alkali-rich nephelinitic evolved magmas after protracted differentiation. Radiogenic isotopes help to distinguish which magmatic series has a petrogenetic link with the differentiated alkali-rich melts. Olivine melilitites are depleted in Sr radiogenic isotopes (⁸⁷Sr/⁸⁶Sr in olivine melilitites ~0.7037 vs. ~0.7042–0.705 in alkali-rich nephelinites and phonolites; Keller et al., 2006), depleted in Nd radiogenic isotopes (¹⁴³Nd/¹⁴⁴Nd ~0.5128 in olivine melilitites, ~0.5125–0.5127 in alkali-rich nephelinites and phonolites) and enriched in Pb radiogenic isotopes (²⁰⁶Pb/²⁰⁴Pb ~ 19.8–20 in olivine melilitites, ~18–19.3 in alkali-rich nephelinites and phonolites) compared to alkali-rich nephelinites and phonolite lavas from the Oldoinyo Lengai (Keller et al., 2006). Radiogenic isotopes suggest that olivine melilitites and phonolites do not have a common mantle source. Alkali-rich nephelinites, olivine melilitites and phonolites are isotopically defined by various degrees of mixing (or contamination) between an enriched lithosphere (called 'EM1') and the HIMU end-member (Keller et al., 2006). Dawson (2012) proposed that the interaction of a low fraction of olivine melilitite melt, produced by the melting of a carbonated peridotite, with a larger fraction of carbonated peridotitic melt, can produce alkali-rich nephelinite melts. Alkali-rich nephelinites are, therefore, inferred to be produced by the contamination with a carbonated lithosphere (Dawson, 2012).

On the other hand, olivine nephelinites are assumed to result from a low degree of partial melting (up to 1%) of a carbonate-rich garnet peridotite with ~2 vol % phlogopite (e.g. olivine nephelinite from the Manyara-Balangida rift, Tanzania; Baudouin & Parat, 2020). To our knowledge, no radiogenic isotopic data is available for the olivine nephelinite lavas to demonstrate whether or not olivine nephelinites have a petrogenetic link with phonolites and natrocarbonatites. Mollex et al. (2018) have suggested, based on the helium isotopic composition of one of the xenoliths studied herein, from the Embalulu Oltatwa crater, that the crystallized magma had no crustal contamination during the rise of the magma to the surface. Thus, the study of primitive xenoliths from Embalulu Oltatwa crater provides us with a good proxy of the composition and processes associated with relatively primitive melts that are present at deep crustal levels beneath the Oldoinyo Lengai volcano. We consider that the MIs with an olivine nephelinite composition are not contaminated and give insights into the primitive melts under Oldoinyo Lengai. To understand the petrogenetic link between silica-undersaturated olivine nephelinite and alkali-rich phonolite magmas both formed at Oldoinyo Lengai, we performed Rhyolite-MELTS model (v.1.2.0; Ghiorso & Gualda, 2015) calculations (Fig. 14) aiming at constraining the role of H₂O, pressure and oxygen fugacity (fO₂) regime during fractional crystallization of olivine nephelinites. The starting composition used for the calculations is reported in Table 3 and corresponds to the average MIs corrected for PEC. We considered two oxygen fugacity end-members (FMQ 0 and FMQ + 2), two pressures (400 MPa and 1 GPa, representing shallow and deep crustal reservoirs), and two H₂O contents (1 wt % and 1.4 wt % H₂O, overlapping concentrations measured in MIs). The starting composition (reported in Table 3) is identical for all the models presented in Fig. 14. At low temperatures (<850°C), three models (400 MPa/FMQ + 2/1 wt % H₂O; 400 MPa/FMQ + 2/1.4 wt % H₂O; 1 GPa/FMQ + 2/1.4 wt % H₂O) produce melt compositions resembling low-alkali phonolite lavas from Oldoinyo Lengai (Na₂O + K₂O vs. SiO₂ diagram in Fig. 14c). Models with melts containing the most alkalis at low temperature are those with initial conditions set at 400 MPa/FMQ/1 wt % H₂O and 1 GPa/FMQ/1 wt % H₂O. More generally, Rhyolite-MELT models highlight a possible petrogenetic link between olivine nephelinitic melts and alkaline melts by fractional crystallization. Fractional crystallization of an olivine nephelinitic melt can thus reproduce the high Na + K contents (up to 18 wt % Na₂O + K₂O) measured in phonolites alkaline rocks from Oldoinyo Lengai, those that are immiscible with alkaline carbonatites. For instance, fractional crystallization of 80% of an initial olivine nephelinitic melt (with an initial melt CO₂ concentration of 0.6 wt %) leads to a phonolitic melt with ~3 wt % CO₂ (assuming CO₂ as fully incompatible). Such a high C content is consistent with the CO₂ concentration of highly alkaline silicate melts that are equilibrated with carbonatites from Oldoinyo Lengai (de Moor et al., 2013). Fractionation of such alkaline Si-undersaturated parent melts causes the evolving melt to become enriched with alkali and CO₂. This enrichment ultimately likely leads to the carbonate-silicate immiscibility (Weidendorfer et al., 2016).

Olivine nephelinitic and melilititic melts are two separate series (e.g. Ca content measured in olivine melilititic rocks is in general higher than for olivine nephelinitic rocks; Fig. 14b) that are not related by fractional crystallization of a common melt. We propose that the phonolite alkaline rocks from Oldoinyo Lengai are produced by protracted differentiation of olivine nephelinitic melts.

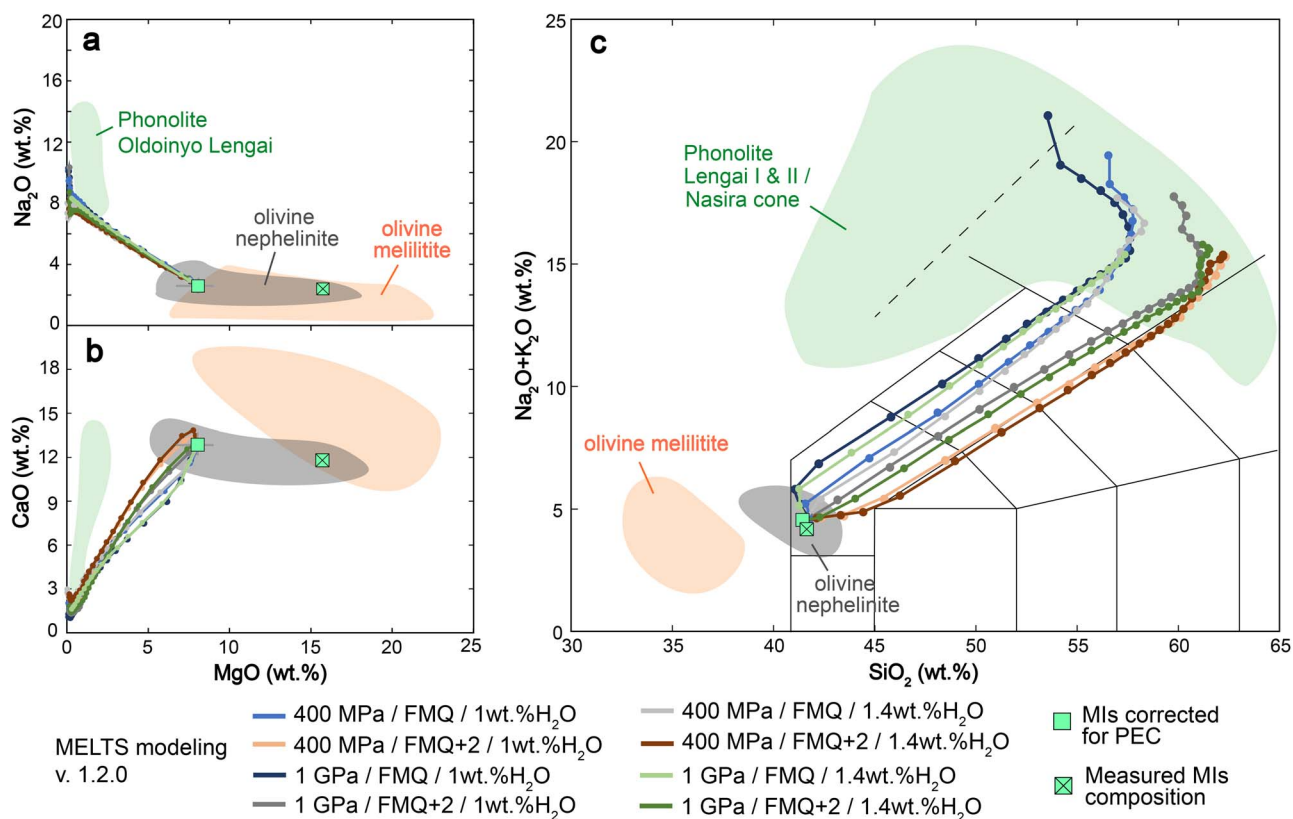


Fig. 14. Modeling the liquid line of descent (fractional crystallization) for the Mg-nephelinite suites using Rhyolite-MELTS v.1.2.0 (Ghiorso & Gualda, 2015). We considered two oxygen fugacity end-members (FMQ and FMQ+2), two pressures (400 MPa and 1 GPa representing shallow and deep crustal depths), and two H₂O contents (1 σ H₂O variation measured in olivine-hosted melt inclusions). The starting composition is reported in Table 3. Fields for phonolites, olivine nephelinites and olivine melilitites are whole-rock compositions retrieved from Mattsson et al. (2013). Models highlight a possible petrogenetic link between olivine nephelinitic melts and alkaline melts by fractional crystallization. Olivine nephelinitic and olivine melilitic melts are two separate series that are not related by fractional crystallization of a common melt.

Table 3: Starting composition used for the MELTS models

Element	Starting composition (w. %)
SiO ₂	41.72
TiO ₂	4.32
Al ₂ O ₃	11.50
Fe ₂ O ₃	3.15
FeO	12.28
MgO	8.15
CaO	13.00
Na ₂ O	2.63
K ₂ O	1.95
P ₂ O ₅	0.20

CONCLUSION

Xenoliths from the Oltatwa tuff ring on the east flank of Oldoinyo Lengai allow evaluation of the early stage of magma differentiation in an active carbonatitic complex. We discussed the global evolution of the primitive melts beneath the volcano in terms of mineral textures, composition (major, trace and volatile contents), as well as crystallization conditions (pressure, temperature). Xenoliths are composed of olivine, diopside, phlogopite, amphibole and accessory minerals. One remarkable feature is the presence of diopside and phlogopite oikocrysts enclosing roundish partially resorbed olivine chadacrysts. MIs have an olivine nephelinite major composition. Olivine-hosted

MIs are poor in S (<130 ppm), relatively rich in Cl (up to 540 ppm) and rich in F (up to 4500 ppm). The volatile content of those MIs and the presence of hydrous phases (i.e. phlogopite and amphibole) in the xenoliths confirm that the lithospheric mantle beneath Oldoinyo Lengai is highly metasomatized. Primitive olivine nephelinite MIs have slightly higher H₂O content (up to 1.5 wt % H₂O) than H₂O content in olivine nephelinite lavas from other volcanoes from the North Tanzanian Divergence, suggesting that the lithospheric mantle source beneath the Oldoinyo Lengai is slightly more hydrated than the mantle beneath the North Tanzanian Divergence. We present a model in which dissolution features observed in olivine chadacrysts, together with the LREE enrichments in some olivine grains, are the consequences of intense reactive porous flows in a deep crustal mushy reservoir. Finally, Rhyolite-MELTS models showed that phonolites and related alkaline carbonatites from Oldoinyo Lengai can be produced by protracted differentiation of olivine nephelinite melts.

Acknowledgements

The authors thank Olivier Bruguier (Geosciences Montpellier) for analytical support, Fabrice Barou for EBSD measurements, Christophe Nevado for thin section preparation, Olivier Rouer for access to EMPA, Céline Baudouin (Geosciences Montpellier, CRPG) for her introduction to the GLITTER software to AM and for numerous discussions related to the Natron Igneous Province

with LF. We are grateful to the following persons from Laboratoire Magmas et Volcans (Clermont-Ferrand) for their technical assistance: Claire Fonquernie (CHNS elemental analysis), Federica Schiavi (FTIR spectroscopy), Mhammed Benbakkar (ICP-AES), Jean-Luc Devidal (LA-ICP MS). We also thank the Tanzania Commission for Science and Technology (COSTECH) for field permits and Emmanuel Kazimoto from Dar Es Salaam University for assistance during field work. The authors thank the reviewers Márta Berkesi and Tobias Fischer and editor Mary Reid for the numerous insightful and constructive comments, which helped improve the original version of the manuscript significantly.

Funding

This work has been supported by the French National Research Agency through the national program 'Investissements d'avenir' with the reference ANR-10-LABX-21-01/LABEX RESSOURCES21 and through the project GECO-REE (ANR-16-CE01-0003-01) to LF. We also thank the contribution of the Région Lorraine, PNP and CESSUR programs from INSU-CNRS. This is CRPG contribution #2852, and GECO-REE contribution #9.

Conflict of interest

The authors declare no conflicts of interest.

References

- Aiuppa, A., Baker, D. R. & Webster, J. D. (2009). Halogens in volcanic systems. *Chemical Geology* **263**, 1–18. <https://doi.org/10.1016/j.chemgeo.2008.10.005>.
- Albaric, J., Perrot, J., Déverchère, J., Deschamps, A., Le Gall, B., Ferdinand, R. W., Petit, C., Tiberi, C., Sue, C. & Songu, M. (2010). Contrasted seismogenic and rheological behaviours from shallow and deep earthquake sequences in the north Tanzanian divergence, East Africa. *Journal of African Earth Sciences* **58**(5), 799–811. <https://doi.org/10.1016/j.jafrearsci.2009.09.005>.
- Arai, S. (1986). K/Na variation in phlogopite and amphibole of upper mantle peridotites due to fractionation of the metasomatizing fluids. *Journal of Geology* **94**(3), 436–444. <https://doi.org/10.1086/629042>.
- Atlas, Z. D., Dixon, J. E., Sen, G., Finny, M. & Martin-Del Pozzo, A. L. (2006). Melt inclusions from Volcán Popocatepetl and Volcán de Colima, Mexico: melt evolution due to vapor-saturated crystallization during ascent. *Journal of Volcanology and Geothermal Research* **153**(3–4), 221–240. <https://doi.org/10.1016/j.jvolgeores.2005.06.010>.
- Basch, V., Rampone, E., Crispini, L., Ferrando, C., Ildefonse, B. & Godard, M. (2018). From mantle peridotites to hybrid troctolites: textural and chemical evolution during melt-rock interaction history (Mt. Maggiore, Corsica, France). *Lithos* **323**, 4–23. <https://doi.org/10.1016/j.lithos.2018.02.025>.
- Baudouin, C. & France, L. (2019). Trace element partitioning between wollastonite and alkaline silicate magmas. *Chemical Geology* **523**, 88–94. <https://doi.org/10.1016/j.chemgeo.2019.06.001>.
- Baudouin, C. & Parat, F. (2020). Phlogopite-olivine nephelinites erupted during early stage rifting, north Tanzanian divergence. *Frontiers in Earth Science* **8**, 277. <https://doi.org/10.3389/feart.2020.00277>.
- Baudouin, C., France, L., Boulanger, M., Dalou, C. & Devidal, J. L. (2020). Trace element partitioning between clinopyroxene and alkaline magmas: parametrization and role of M1 site on HREE enrichment in clinopyroxenes. *Contributions to Mineralogy and Petrology* **175**, 1–15. <https://doi.org/10.1007/s00410-020-01680-6>.
- Beattie, P. (1993). Olivine-melt and orthopyroxene-melt equilibria. *Contributions to Mineralogy and Petrology* **115**(1), 103–111. <https://doi.org/10.1007/BF00712982>.
- Bell, K. & Simonetti, A. (2010). Source of parental melts to carbonatites-critical isotopic constraints. *Mineralogy and Petrology* **98**, 77–89. <https://doi.org/10.1007/s00710-009-0059-0>.
- Berkesi, M., Myovela, J. L., Yaxley, G. M. & Guzmics, T. (2023). Carbonatite formation in continental settings via high pressure–high temperature liquid immiscibility. *Geochimica et Cosmochimica Acta* **349**, 41–54. <https://doi.org/10.1016/j.gca.2023.03.027>.
- Blundy, J., Cashman, K. V., Rust, A. & Witham, F. (2010). A case for CO₂-rich arc magmas. *Earth and Planetary Science Letters* **290**(3–4), 289–301. <https://doi.org/10.1016/j.epsl.2009.12.013>.
- Bosshard-Stadlin, S. A., Mattsson, H. B. & Keller, J. (2014). Magma mixing and forced exsolution of CO₂ during the explosive 2007–2008 eruption of Oldoinyo Lengai (Tanzania). *Journal of Volcanology and Geothermal Research* **285**, 229–246. <https://doi.org/10.1016/j.jvolgeores.2014.08.017>.
- Bouilhol, P., Schmidt, M. W. & Burg, J. P. (2015). Magma transfer and evolution in channels within the arc crust: the pyroxenitic feeder pipes of Sapat (Kohistan, Pakistan). *Journal of Petrology* **56**(7), 1309–1342. <https://doi.org/10.1093/petrology/egv037>.
- Boulanger, M. & France, L. (2023). Cumulate formation and melt extraction from mush-dominated magma reservoirs: the melt flush process exemplified at mid-ocean ridges. *Journal of Petrology* **64**(2), egad005. <https://doi.org/10.1093/petrology/egad005>.
- Boulanger, M., France, L., Deans, J. R., Ferrando, C., Lissenberg, C. J. & Von Der Handt, A. (2020). Magma reservoir formation and evolution at a slow-spreading center (Atlantis Bank, southwest Indian ridge). *Frontiers in Earth Science* **8**, 554598. <https://doi.org/10.3389/feart.2020.554598>.
- Boulanger, M., France, L., Ferrando, C., Ildefonse, B., Ghosh, B., Sanfilippo, A., Liu, C.-Z., Morishita, T., Koepke, J. & Bruguier, O. (2021). Magma-mush interactions in the lower oceanic crust: insights from Atlantis Bank layered series (southwest Indian ridge). *Journal of Geophysical Research: Solid Earth* **126**(9), e2021JB022331.
- Brooker, R. A., Kohn, S. C., Holloway, J. R. & McMillan, P. F. (2001). Structural controls on the solubility of CO₂ in silicate melts: part I: bulk solubility data. *Chemical Geology* **174**(1–3), 225–239. [https://doi.org/10.1016/S0009-2541\(00\)00353-3](https://doi.org/10.1016/S0009-2541(00)00353-3).
- Bucholz, C. E., Gaetani, G. A., Behn, M. D. & Shimizu, N. (2013). Post-entrapment modification of volatiles and oxygen fugacity in olivine-hosted melt inclusions. *Earth and Planetary Science Letters* **374**, 145–155. <https://doi.org/10.1016/j.epsl.2013.05.033>.
- Buso, R., Laporte, D., Schiavi, F., Cluzel, N. & Fonquernie, C. (2022). High-pressure homogenization of olivine-hosted CO₂-rich melt inclusions in a piston cylinder: insight into the volatile content of primary mantle melts. *European journal of mineralogy special volume: experiments and mineral physics at mantle depths. European Journal of Mineralogy* **34**, 325–349. <https://doi.org/10.5194/ejrm-34-325-2022>.
- Caricchi, L., Sheldrake, T. E. & Blundy, J. (2018). Modulation of magmatic processes by CO₂ flushing. *Earth and Planetary Science Letters* **491**, 160–171. <https://doi.org/10.1016/j.epsl.2018.03.042>.
- Cashman, K. V., Sparks, R. S. J. & Blundy, J. D. (2017). Vertically extensive and unstable magmatic systems: a unified view of igneous processes. *Science* **355**(6331), eaag3055. <https://doi.org/10.1126/science.aag3055>.
- Casola, V., France, L., Galy, A., Bouden, N. & Villeneuve, J. (2020). No evidence for carbon enrichment in the mantle source of

- carbonatites in eastern Africa. *Geology* **48**, 971–975. <https://doi.org/10.1130/g47629.1>.
- Clutier, A., Gautier, S. & Tiberi, C. (2021). Hybrid local and teleseismic P-wave tomography in North Tanzania: role of inherited structures and magmatism on continental rifting. *Geophysical Journal International* **224**(3), 1588–1606. <https://doi.org/10.1093/gji/ggaa538>.
- Connors, L., Wallace, P. J., Sims, K. W. W., Sublett, D. M., Jr. & Bodnar, R. J. (2020). Tracing the sources of CO₂-rich magmas at Nyiragongo and Nyamulagira using olivine-hosted melt inclusions. American Geophysical Union, fall meeting 2020. abstract #V026-02.
- Cooper, G. F., Davidson, J. P. & Blundy, J. D. (2016). Plutonic xenoliths from Martinique, Lesser Antilles: evidence for open system processes and reactive melt flow in island arc crust. *Contributions to Mineralogy and Petrology* **171**, 1–21. <https://doi.org/10.1007/s00410-016-1299-8>.
- Danyushevsky, L. V. (2001). The effect of small amounts of H₂O on crystallization of mid ocean ridge and back arc basin magmas. *Journal of Volcanology and Geothermal Research* **110**, 265–280. [https://doi.org/10.1016/S0377-0273\(01\)00213-X](https://doi.org/10.1016/S0377-0273(01)00213-X).
- Danyushevsky, L. V. & Plechov, P. (2011). Petrolog3: integrated software for modeling crystallization processes. *Geochemistry, Geophysics, Geosystems* **12**, Q07021. <https://doi.org/10.1029/2011gc003516>.
- Dawson, J. B. (1992). Neogene tectonics and volcanicity in the north Tanzania sector of the Gregory Rift valley: contrasts with the Kenya sector. *Tectonophysics* **204**(1–2), 81–92. [https://doi.org/10.1016/0040-1951\(92\)90271-7](https://doi.org/10.1016/0040-1951(92)90271-7).
- Dawson, J. B. (1998). Peralkaline nephelinite–natrocarbonate relationships at Oldoinyo Lengai. *Tanzania. Journal of Petrology* **39**(11–12), 2077–2094. <https://doi.org/10.1093/ptro/39.11-12.2077>.
- Dawson, J. B. (2012). Nephelinite–melilitite–carbonate relationships: evidence from Pleistocene–recent volcanism in northern Tanzania. *Lithos* **152**, 3–10. <https://doi.org/10.1016/j.lithos.2012.01.008>.
- Dawson, J. B. & Smith, J. V. (1988). Metasomatized and veined upper-mantle xenoliths from Pello Hill, Tanzania: evidence for anomalously-light mantle beneath the Tanzanian sector of the east African Rift Valley. *Contributions to Mineralogy and Petrology* **100**, 510–527. <https://doi.org/10.1007/bf00371380>.
- Dawson, J. B. & Smith, J. V. (1992). Olivine-mica pyroxenite xenoliths from northern Tanzania: metasomatic products of upper-mantle peridotite. *Journal of Volcanology and Geothermal Research* **50**(1–2), 131–142. [https://doi.org/10.1016/0377-0273\(92\)90041-B](https://doi.org/10.1016/0377-0273(92)90041-B).
- Dawson, J. B., Smith, J. V. & Steele, I. M. (1995). Petrology and mineral chemistry of plutonic igneous xenoliths from the carbonate volcano, Oldoinyo Lengai. *Tanzania. Journal of Petrology* **36**(3), 797–826. <https://doi.org/10.1093/petrology/36.3.797>.
- Dixon, J. E. (1997). Degassing of alkalic basalts. *American Mineralogist* **82**(3–4), 368–378. <https://doi.org/10.2138/am-1997-3-415>.
- Faure, F., Trolliard, G., Nicollet, C. & Montel, J. M. (2003). A developmental model of olivine morphology as a function of the cooling rate and the degree of undercooling. *Contributions to Mineralogy and Petrology* **145**, 251–263. <https://doi.org/10.1007/s00410-003-0449-y>.
- Ferrando, C., Basch, V., Ildefonse, B., Deans, J., Sanfilippo, A., Barou, F. & France, L. (2021a). Role of compaction in melt extraction and accumulation at a slow spreading center: microstructures of olivine gabbros from the Atlantis Bank (IODP hole U1473A, SWIR). *Tectonophysics* **815**, 229001. <https://doi.org/10.1016/j.tecto.2021.229001>.
- Ferrando, C., France, L., Basch, V., Sanfilippo, A., Tribuzio, R. & Boulanger, M. (2021b). Grain size variations record segregation of residual melts in slow-spreading oceanic crust (Atlantis Bank, 57° E southwest Indian ridge). *Journal of geophysical research: solid. Earth* **126**(4), e2020JB020997. <https://doi.org/10.1029/2020JB020997>.
- Fischer, T. P., Burnard, P., Marty, B., Hilton, D. R., Füre, E., Palhol, F., Sharp, Z. D. & Mangasini, F. (2009). Upper-mantle volatile chemistry at Oldoinyo Lengai volcano and the origin of carbonatites. *Nature* **459**(7243), 77–80. <https://doi.org/10.1038/nature07977>.
- Fischer, L. A., Erdmann, M., France, L., Wolff, P. E., Delouie, E., Zhang, C. & Koepke, J. (2016). Trace element evidence for anatexis at oceanic magma chamber roofs and the role of partial melts for contamination of fresh MORB. *Lithos* **260**, 1–8. <https://doi.org/10.1016/j.lithos.2016.05.001>.
- France, L., Koepke, J., MacLeod, C. J., Ildefonse, B., Godard, M. & Delouie, E. (2014). Contamination of MORB by anatexis of magma chamber roof rocks: constraints from a geochemical study of experimental melts and associated residues. *Lithos* **202–203**, 120–137. <https://doi.org/10.1016/j.lithos.2014.05.018>.
- France, L., Brouillet, F. & Lang, S. (2021). Early carbonate magmatism at Oldoinyo Lengai volcano (Tanzania): carbonate–silicate melt immiscibility in Lengai I melt inclusions. *Comptes Rendus Géosciences* **353**(S2), 273–288.
- Frezzotti, M. L. (2001). Silicate-melt inclusions in magmatic rocks: applications to petrology. *Lithos* **55**(1–4), 273–299. [https://doi.org/10.1016/S0024-4937\(00\)00048-7](https://doi.org/10.1016/S0024-4937(00)00048-7).
- Gaetani, G. A., O’Leary, J. A., Shimizu, N., Bucholz, C. E. & Newville, M. (2012). Rapid reequilibration of H₂O and oxygen fugacity in olivine-hosted melt inclusions. *Geology* **40**, 915–918. <https://doi.org/10.1130/G32992.1>.
- Gagnon, J. E., Fryer, B. J., Samson, I. M. & Williams-Jones, A. E. (2008). Quantitative analysis of silicate certified reference materials by LA-ICPMS with and without an internal standard. *Journal of Analytical Atomic Spectrometry* **23**(11), 1529–1537. <https://doi.org/10.1039/b801807n>.
- Ghiorso, M. S. & Gualda, G. A. (2015). An H₂O–CO₂ mixed fluid saturation model compatible with rhyolite-melts. *Contributions to Mineralogy and Petrology* **169**(6), 1–30. <https://doi.org/10.1007/s00410-015-1141-8>.
- Gleeson, M. L., Gibson, S. A. & Stock, M. J. (2021). Upper mantle mush zones beneath low melt flux ocean island volcanoes: insights from Isla Floreana, Galápagos. *Journal of Petrology* **61**(11–12), egaa094. <https://doi.org/10.1093/petrology/egaa094>.
- Günther, D., Frischknecht, R., Heinrich, C. A. & Kahlert, H. J. (1997). Capabilities of an argon fluoride 193 nm excimer laser for laser ablation inductively coupled plasma mass spectrometry microanalysis of geological materials. *Journal of Analytical Atomic Spectrometry* **12**(9), 939–944. <https://doi.org/10.1039/A701423F>.
- Halász, N., Berkesi, M., Tóth, T. M., Mitchell, R. H., Milke, R. & Guzmics, T. (2023). Reconstruction of magma chamber processes preserved in olivine-phlogopite micro-ijolites from the Oldoinyo Lengai. *Tanzania. Journal of African Earth Sciences* **197**, 104738. <https://doi.org/10.1016/j.jafrearsci.2022.104738>.
- Hammouda, T., Chantel, J., Manthilake, G., Guignard, J. & Crichton, W. (2014). Hot mantle geotherms stabilize calcic carbonate magmas up to the surface. *Geology* **42**(10), 911–914. <https://doi.org/10.1130/g35778.1>.
- Hauri, E., Wang, J., Dixon, J. E., King, P. L., Mandeville, C. & Newman, S. (2002). SIMS analysis of volatiles in silicate glasses: 1. Calibration, matrix effects and comparisons with FTIR. *Chemical Geology* **183**(1–4), 99–114. [https://doi.org/10.1016/S0009-2541\(01\)00375-8](https://doi.org/10.1016/S0009-2541(01)00375-8).

- Hirschmann, M. M. (2010). Partial melt in the oceanic low velocity zone. *Physics of the Earth and Planetary Interiors* **179**(1–2), 60–71. <https://doi.org/10.1016/j.pepi.2009.12.003>.
- Iacono-Marziano, G., Morizet, Y., Le Trong, E. & Gaillard, F. (2012). New experimental data and semi-empirical parameterization of H₂O–CO₂ solubility in mafic melts. *Geochimica et Cosmochimica Acta* **97**, 1–23. <https://doi.org/10.1016/j.gca.2012.08.035>.
- Iacovino, K., Matthews, S., Wieser, P. E., Moore, G. & Bégué, F. (2021). Vesical part I: an open-source thermodynamic model engine for mixed volatile (H₂O–CO₂) solubility in silicate melts. *Earth and Space Science* **8**(11), e2020EA001584. <https://doi.org/10.1029/2020EA001584>.
- Ismail, W. B. & Mainprice, D. (1998). An olivine fabric database: an overview of upper mantle fabrics and seismic anisotropy. *Tectonophysics* **296**(1–2), 145–157. [https://doi.org/10.1016/s0040-1951\(98\)00141-3](https://doi.org/10.1016/s0040-1951(98)00141-3).
- Jambon, A., Déruelle, B., Dreibus, G. & Pineau, F. (1995). Chlorine and bromine abundance in MORB: the contrasting behaviour of the mid-Atlantic ridge and East Pacific rise and implications for chlorine geodynamic cycle. *Chemical Geology* **126**, 101–117. [https://doi.org/10.1016/0009-2541\(95\)00112-4](https://doi.org/10.1016/0009-2541(95)00112-4).
- Johnson, E. R., Wallace, P. J., Cashman, K. V., Granados, H. D. & Kent, A. J. (2008). Magmatic volatile contents and degassing-induced crystallization at Volcán Jorullo, Mexico: implications for melt evolution and the plumbing systems of monogenetic volcanoes. *Earth and Planetary Science Letters* **269**(3–4), 478–487. <https://doi.org/10.1016/j.epsl.2008.03.004>.
- Keller, J., Zaitsev, A. & Wiedenmann, D. (2006). Primary magmas at Oldoinyo Lengai: the role of olivine melilitites. *Lithos* **91**(1–4), 150–172. <https://doi.org/10.1016/j.lithos.2006.03.014>.
- Keller, J., Klaudius, J., Kervyn, M., Ernst, G. G. & Mattsson, H. B. (2010). Fundamental changes in the activity of the natrocarbonatite volcano Oldoinyo Lengai, Tanzania: I. New magma composition during the 2007–2008 explosive eruptions. *Bulletin of Volcanology* **72**, 893–912. <https://doi.org/10.1007/s00445-010-0371-x>.
- Kervyn, M., Ernst, G. G., Keller, J., Vaughan, R. G., Klaudius, J., Pradal, E., Belton, F., Mattsson, H. B., Mbede, E. & Jacobs, P. (2010). Fundamental changes in the activity of the natrocarbonatite volcano Oldoinyo Lengai, Tanzania. *Bulletin of Volcanology* **72**(8), 913–931. <https://doi.org/10.1007/s00445-010-0360-0>.
- Klaudius, J. & Keller, J. (2006). Peralkaline silicate lavas at Oldoinyo Lengai, Tanzania. *Lithos* **91**(1–4), 173–190. <https://doi.org/10.1016/j.lithos.2006.03.017>.
- Lang, S., Mollo, S., France, L., Misiti, V. & Nazzari, M. (2021). Kinetic partitioning of major-minor cations between olivine and Hawaiian tholeiitic basalt under variable undercooling and cooling rate conditions. *Chemical Geology* **584**, 120485. <https://doi.org/10.1016/j.chemgeo.2021.120485>.
- Le Bas, M. J. (1989). Nephelinitic and basanitic rocks. *Journal of Petrology* **30**, 1299–1312. <https://doi.org/10.1093/petrology/30.5.1299>.
- Lerner, A. H., Wallace, P. J., Shea, T., Mourey, A. J., Kelly, P. J., Nadeau, P. A. & Werner, C. A. (2021). The petrologic and degassing behavior of sulfur and other magmatic volatiles from the 2018 eruption of Kilauea, Hawai'i: melt concentrations, magma storage depths, and magma recycling. *Bulletin of Volcanology* **83**(6), 43. <https://doi.org/10.1007/s00445-021-01459-y>.
- Li, H. & Zhang, L. (2022). A thermodynamic model for sulfur content at sulfide saturation (SCSS) in hydrous silicate melts: with implications for arc magma genesis and sulfur recycling. *Geochimica et Cosmochimica Acta* **325**, 187–204. <https://doi.org/10.1016/j.gca.2022.03.008>.
- Lissenberg, C. J. & Dick, H. J. (2008). Melt–rock reaction in the lower oceanic crust and its implications for the genesis of mid-ocean ridge basalt. *Earth and Planetary Science Letters* **271**(1–4), 311–325. <https://doi.org/10.1016/j.epsl.2008.04.023>.
- MacLennan, J. (2017). Bubble formation and decrepitation control the CO₂ content of olivine-hosted melt inclusions. *Geochemistry, Geophysics, Geosystems* **18**(2), 597–616. <https://doi.org/10.1002/2016GC006633>.
- Mainprice, D., Bachmann, F., Hielscher, R. & Schaeben, H. (2014). Descriptive tools for the analysis of texture projects with large datasets using MTEX: strength, symmetry and components. *Geological Society London, Special Publications* **409**(1), 251–271. <https://doi.org/10.1144/sp409.8>.
- Mangler, M. F., Marks, M. A., Zaitzev, A. N., Eby, G. N. & Markl, G. (2014). Halogens (F, Cl and Br) at Oldoinyo Lengai volcano (Tanzania): effects of magmatic differentiation, silicate–natrocarbonatite melt separation and surface alteration of natrocarbonatite. *Chemical Geology* **365**, 43–53. <https://doi.org/10.1016/j.chemgeo.2013.11.027>.
- Marschall, H. R., Wanless, V. D., Shimizu, N., Pogge von Strandmann, P. A. E., Elliott, T. & Monteleone, B. D. (2017). The boron and lithium isotopic composition of mid-ocean ridge basalts and the mantle. *Geochimica et Cosmochimica Acta* **207**, 102–138. <https://doi.org/10.1016/j.gca.2017.03.028>.
- Mattsson, H. B. (2012). Rapid magma ascent and short eruption durations in the Lake Natron–Engaruka monogenetic volcanic field (Tanzania): a case study of the olivine melilititic Pello Hill scoria cone. *Journal of Volcanology and Geothermal Research* **247–248**, 16–25. <https://doi.org/10.1016/j.jvolgeores.2012.07.009>.
- Mattsson, H. B., Nandedkar, R. H. & Ulmer, P. (2013). Petrogenesis of the melilititic and nephelinitic rock suites in the Lake Natron–Engaruka monogenetic volcanic field, northern Tanzania. *Lithos* **179**, 175–192. <https://doi.org/10.1016/j.lithos.2013.07.012>.
- McDonough, W. F. & Sun, S. S. (1995). The composition of the earth. *Chemical Geology* **120**, 223–253. [https://doi.org/10.1016/0009-2541\(94\)00140-4](https://doi.org/10.1016/0009-2541(94)00140-4).
- Métrich, N. & Wallace, P. (2008). Volatile abundances in basaltic magmas and their degassing paths tracked by melt inclusions. *Reviews in Mineralogy and Geochemistry* **69**(1), 363–402. <https://doi.org/10.1515/9781501508486-011>.
- Milman-Barris, M. S., Beckett, J. R., Baker, M. B., Hofmann, A. E., Morgan, Z., Crowley, M. R. & Stolper, E. (2008). Zoning of phosphorus in igneous olivine. *Contributions to Mineralogy and Petrology* **155**, 739–765. <https://doi.org/10.1007/s00410-007-0268-7>.
- Mitchell, R. H. (2009). Peralkaline nephelinitic–natrocarbonatite immiscibility and carbonatite assimilation at Oldoinyo Lengai, Tanzania. *Contributions to Mineralogy and Petrology* **158**(5), 589–598. <https://doi.org/10.1007/s00410-009-0398-1>.
- Mollex, G., Füre, E., Burnard, P., Zimmermann, L., Chazot, G., Kazimoto, E. O., Marty, B. & France, L. (2018). Tracing helium isotope compositions from mantle source to fumaroles at Oldoinyo Lengai volcano, Tanzania. *Chemical Geology* **480**, 66–74. <https://doi.org/10.1016/j.chemgeo.2017.08.015>.
- de Moor, J. M., Fischer, T. P., King, P. L., Botcharnikov, R. E., Hervig, R. L., Hilton, D. R. & Ramirez, C. (2013). Volatile-rich silicate melts from Oldoinyo Lengai volcano (Tanzania): implications for carbonatite genesis and eruptive behavior. *Earth and Planetary Science Letters* **361**, 379–390. <https://doi.org/10.1016/j.epsl.2012.11.006>.
- Mourey, A. J. & Shea, T. (2019). Forming olivine phenocrysts in basalt: a 3D characterization of growth rates in laboratory experiments. *Frontiers in Earth Science* **7**, 300. <https://doi.org/10.3389/feart.2019.00300>.
- Mourey, A. J., Shea, T. & Hammer, J. E. (2023). Preservation of magma recharge signatures in Kilauea olivine during protracted stor-

- age. *Journal of Geophysical Research: Solid Earth* **128**. <https://doi.org/10.1029/2022JB025523>.
- Nabyl, Z., Massuyeau, M., Gaillard, F., Tuduri, J., Iacono-Marziano, G., Rogerie, G. & Bailly, L. (2020). A window in the course of alkaline magma differentiation conducive to immiscible REE-rich carbonatites. *Geochimica et Cosmochimica Acta* **282**, 297–323. <https://doi.org/10.1016/j.gca.2020.04.008>.
- Newman, S. & Lowenstern, J. B. (2002). Volatilecalc: a silicate melt–H₂O–CO₂ solution model written in visual basic for excel. *Computers and Geosciences* **28**(5), 597–604. [https://doi.org/10.1016/S0098-3004\(01\)00081-4](https://doi.org/10.1016/S0098-3004(01)00081-4).
- O'Neill, H. S. C. (2021). The thermodynamic controls on sulfide saturation in silicate melts with application to ocean floor basalts. *Magma Redox Geochemistry*, 177–213. <https://doi.org/10.1002/9781119473206.ch10>.
- Peterson, T. D. (1989). Peralkaline nephelinites. I. Comparative petrology of Shombole and Oldoinyo L'engai, East Africa. *Contributions to Mineralogy and Petrology* **101**(4), 458–478. <https://doi.org/10.1007/BF00372219>.
- Plasman, M., Tiberi, C., Ebinger, C., Gautier, S., Albaric, J., Peyrat, S., Déverchère, J., Le Gall, B., Tarits, P., Roecker, S., Wambura, F., Muzuka, A., Mulibo, G., Mtelela, K., Msabi, M., Kianji, G., Hautot, S., Perrot, J. & Gama, R. (2017). Lithospheric low-velocity zones associated with a magmatic segment of the Tanzanian rift, East Africa. *Geophysical Journal International* **210**(1), 465–481. <https://doi.org/10.1093/gji/ggx177>.
- Pouchou, J.-L. & Pichoir, F. (1991). Quantitative analysis of homogeneous or stratified microvolumes applying the model "PAP". *Electron Probe Quantification*, 31–75. https://doi.org/https://doi.org/10.1007/978-1-4899-2617-3_4.
- Processes Mineralogical Society of America. *Reviews in Mineralogy and Geochemistry* **69**, 363–402.
- Pyle, D. M. & Mather, T. A. (2009). Halogens in igneous processes and their fluxes to the atmosphere and oceans from volcanic activity: a review. *Chemical Geology* **263**(1–4), 110–121. <https://doi.org/10.1016/j.chemgeo.2008.11.013>.
- Rasmussen, D. J., Kyle, P. R., Wallace, P. J., Sims, K. W., Gaetani, G. A. & Phillips, E. H. (2017). Understanding degassing and transport of CO₂-rich alkalic magmas at Ross Island, Antarctica using olivine-hosted melt inclusions. *Journal of Petrology* **58**(5), 841–861. <https://doi.org/10.1093/petrology/egx036>.
- Reiss, M. C., Muirhead, J. D., Laizer, A. S., Link, F., Kasimoto, E. O., Ebinger, C. J. & Rumpker, G. (2021). The impact of complex volcanic plumbing on the nature of seismicity in the developing magmatic natron rift, Tanzania. *Frontiers in Earth Science* **8**, 609805. <https://doi.org/10.3389/feart.2020.609805>.
- Roecker, S., Ebinger, C., Tiberi, C., Mulibo, G., Ferdinand-Wambura, R., Mtelela, K., Kianji, G., Muzuka, A., Gautier, S., Albaric, J. & Peyrat, S. (2017). Subsurface images of the eastern rift, Africa, from the joint inversion of body waves, surface waves and gravity: investigating the role of fluids in early-stage continental rifting. *Geophysical Journal International* **210**(2), 931–950. <https://doi.org/10.1093/gji/ggx220>.
- Roedder, E. (1984). Volume 12: fluid inclusions. *Reviews in Mineralogy* **12**, 644.
- Ryan, W. B. F., Carbotte, S. M., Coplan, J. O., O'Hara, S., Melkonian, A., Arko, R., Weissel, R. A., Ferrini, V., Goodwillie, A., Nitsche, F., Bonczkowski, J. & Zemsky, R. (2009). Global multi-resolution topography synthesis. *Geochemistry, Geophysics, Geosystems* **10**(3), Q03014. <https://doi.org/10.1029/2008gc002332>.
- Sekisova, V. S., Sharygin, V. V., Zaitsev, A. N. & Strekopytov, S. (2015). Liquid immiscibility during crystallization of forsterite-ophlogopite ijolites at Oldoinyo Lengai volcano, Tanzania: study of melt inclusions. *Russian Geology and Geophysics* **56**(12), 1717–1737. <https://doi.org/10.1016/j.rgg.2015.11.005>.
- Shea, T., Hammer, J. E., Hellebrand, E., Mourey, A. J., Costa, F., First, E. C., Lynn, K. J. & Melnik, O. (2019). Phosphorus and aluminum zoning in olivine: contrasting behavior of two nominally incompatible trace elements. *Contributions to Mineralogy and Petrology* **174**, 85. <https://doi.org/10.1007/s00410-019-1618-y>.
- Shea, T., Matzen, A. & Mourey, A. J. (2022). Experimental study of Fe–mg partitioning and zoning during rapid growth of olivine in Hawaiian tholeiites. *Contributions to Mineralogy and Petrology* **177**(12), 1–25. <https://doi.org/10.1007/s00410-022-01969-8>.
- Sherrod, D. R., Magitita, M. M. & Kwelwa, S. (2013). Geologic map of Oldoinyo Lengai (Oldoinyo Lengai) and surroundings, Arusha region, United Republic of Tanzania. *United States Geological Survey Open-File Report 2013–1306*. <https://doi.org/10.3133/ofr20131306>.
- Shishkina, T. A., Botcharnikov, R. E., Holtz, F., Almeev, R. R., Jazwa, A. M. & Jakubiak, A. A. (2014). Compositional and pressure effects on the solubility of H₂O and CO₂ in mafic melts. *Chemical Geology* **388**, 112–129. <https://doi.org/10.1016/j.chemgeo.2014.09.001>.
- Smythe, D. J., Wood, B. J. & Kiseeva, E. S. (2017). The S content of silicate melts at sulfide saturation: new experiments and a model incorporating the effects of sulfide composition. *American Mineralogist* **102**(4), 795–803. <https://doi.org/10.2138/am-2017-5800CCBY>.
- Stamm, N. & Schmidt, M. W. (2017). Asthenospheric kimberlites: volatile contents and bulk compositions at 7 GPa. *Earth and Planetary Science Letters* **474**, 309–321. <https://doi.org/10.1016/j.epsl.2017.06.037>.
- Stronck, N. A. & Haase, K. M. (2004). Chlorine in oceanic intraplate basalts: constraints on mantle sources and recycling processes. *Geology* **32**(11), 945–948. <https://doi.org/10.1130/G21027.1>.
- Tommasi, A., Mainprice, D., Canova, G. & Chastel, Y. (2000). Viscoplastic self-consistent and equilibrium-based modeling of olivine lattice preferred orientations: implications for the upper mantle seismic anisotropy. *Journal of Geophysical Research* **105**(B4), 7893–7908. <https://doi.org/10.1029/1999jb900411>.
- Toplis, M. J. (2005). The thermodynamics of iron and magnesium partitioning between olivine and liquid: criteria for assessing and predicting equilibrium in natural and experimental systems. *Contributions to Mineralogy and Petrology* **149**(1), 22–39. <https://doi.org/10.1007/s00410-004-0629-4>.
- Tournigand, P. Y., Smets, B., Laxton, K., Dille, A., France, L., Chazot, G. & Kervyn, M. (2023). Remote volcano monitoring using crowd-sourced imagery and structure-from-motion photogrammetry: a case study of Oldoinyo Lengai's active pit crater since the 2007–08 paroxysm. *Journal of Volcanology and Geothermal Research* **443**, 107918. <https://doi.org/10.1016/j.jvolgeores.2023.107918>.
- Van Acherbergh, E., Ryan, C., Jackson, S. & Griffin, W. (2001). Data reduction software for LA-ICP-MS. laser ablation-ICPMS in the earth sciences: principles and applications. *Mineralogical Association of Canada (short course series)* **29**, 239–243.
- Verplanck, P. L., Van Gosen, B. S., Seal, R. R., II & McCafferty, A. E. (2014) A deposit model for carbonatite and peralkaline intrusion-related rare earth element deposits: Chapter J in *Mineral deposit models for resource assessment* (No. 2010–5070-J). US Geological Survey, USGS publication.
- Wallace, M. E. & Green, D. H. (1988). An experimental determination of primary carbonatites magma composition. *Nature* **335**, 343–346. <https://doi.org/10.1038/335343a0>.
- Wallace, P. J., Kamenetsky, V. S. & Cervantes, P. (2015). Melt inclusion CO₂ contents, pressures of olivine crystallization, and the problem of shrinkage bubbles. *American Mineralogist* **100**(4), 787–794. <https://doi.org/10.2138/am-2015-5029>.

- Wallace, P. J., Plank, T., Bodnar, R. J., Gaetani, G. A. & Shea, T. (2021). Olivine-hosted melt inclusions: a microscopic perspective on a complex magmatic world. *Annual Review of Earth and Planetary Sciences* **49**, 465–494. <https://doi.org/10.1146/annurev-earth-082420-060506>.
- Weidendorfer, D., Schmidt, M. W. & Mattsson, H. B. (2016). Fractional crystallization of Si-undersaturated alkaline magmas leading to unmixing of carbonatites on Brava Island (Cape Verde) and a general model of carbonatite genesis in alkaline magma suites. *Contributions to Mineralogy and Petrology* **171**, 43. <https://doi.org/10.1007/s00410-016-1249-5>.
- Weidendorfer, D., Schmidt, M. W. & Mattsson, H. B. (2019). Mineral resorption triggers explosive mixed silicate–carbonatite eruptions. *Earth and Planetary Science Letters* **510**, 219–230. <https://doi.org/10.1016/j.epsl.2019.01.003>.
- Weinstein, A., Oliva, S., Ebinger, C., Roecker, S., Tiberi, C., Aman, M., Lambert, C., Witkin, E., Albaric, J., Gautier, S., Peyrat, S., Muirhead, J. D., Muzuka, A. N. N., Mulibo, G., Kianji, G., Ferdinand-Wambura, R., Msabi, M., Rodzianko, A., Hadfield, R., Illsley-Kemp, F. & Fischer, T. P. (2017). Fault-magma interactions during early continental rifting: seismicity of the Magadi-Natron-Manyara basins, Africa. *Geochemistry, Geophysics, Geosystems* **18**(10), 3662–3686. <https://doi.org/10.1002/2017gc007027>.
- Welsch, B., Hammer, J. & Hellebrand, E. (2014). Phosphorus zoning reveals dendritic architecture of olivine. *Geology* **42**(10), 867–870. <https://doi.org/10.1130/G35691.1>.
- Wieser, P. & Gleeson, M. (2022). PySulfSat: an open-source Python3 tool for modelling sulfide and sulfate saturation. *Volcanica* **6**(1), 107–127. <https://doi.org/10.30909/vol.06.01.107127>.
- Wood, B. J. & Blundy, J. D. (1997). A predictive model for rare earth element partitioning between clinopyroxene and anhydrous silicate melt. *Contributions to Mineralogy and Petrology* **129**(2–3), 166–181. <https://doi.org/10.1007/s004100050330>.
- Woolley, A. R. & Kjarsgaard, B. A. (2008). Paragenetic types of carbonatite as indicated by the diversity and relative abundances of associated silicate rocks: evidence from a global database. *Canadian Mineralogist* **46**(4), 741–752. <https://doi.org/10.3749/canmin.46.4.741>.
- Xing, C. M., Wang, C. Y. & Tan, W. (2017). Disequilibrium growth of olivine in mafic magmas revealed by phosphorus zoning patterns of olivine from mafic–ultramafic intrusions. *Earth and Planetary Science Letters* **479**, 108–119. <https://doi.org/10.1016/j.epsl.2017.09.005>.
- Zhang, C., Wang, L. X., Marks, M. A., France, L. & Koepke, J. (2017). Volatiles (CO₂, S, F, Cl, Br) in the dike-gabbro transition zone at IODP hole 1256D: magmatic imprint versus hydrothermal influence at fast-spreading mid-ocean ridge. *Chemical Geology* **459**, 43–60. <https://doi.org/10.1016/j.chemgeo.2017.04.002>.
- Zhu, S. Z., Huang, X. L., Yu, Y., Yang, F., Wang, C. Y., He, P. L. & Cao, J. (2023). Enrichment of incompatible elements in alkaline syenites in large igneous provinces due to magma replenishment and reactive porous flow in a mush reservoir. *Journal of Petrology* **64**(2), egad002. <https://doi.org/10.1093/petrology/egad002>.